A High-Resolution Study of the HI Content of Local Group Dwarf Irregular Galaxy WLM

Amanda A. Kepley and Eric M. Wilcots

Washburn Observatory, University of Wisconsin, 475 North Charter Street, Madison, WI 53706

kepley@astro.wisc.edu,ewilcots@astro.wisc.edu

Deidre A. Hunter

Lowell Observatory, 1400 West Mars Hill Road, Flagstaff, AZ 86001

dah@lowell.edu

Tyler Nordgren

Department of Physics, University of Redlands, 1200 East Colton Avenue, Redlands, CA 92373

tyler_nordgren@redlands.edu

ABSTRACT

Dwarf irregular galaxies are unique laboratories for studying the interaction between stars and the interstellar medium in low mass environments. We present the highest spatial resolution observations to date of the neutral hydrogen content of the Local Group dwarf irregular galaxy WLM. We find that WLM's neutral hydrogen distribution is typical for a galaxy of its type and size and derive an HI mass of $6.3 \pm 0.3 \times 10^7$ $M_\odot$ for WLM. In addition, we derive an HI extent for WLM of $\sim 30'$, which is much less than the $45'$ extent found by Huchtmeier et al. (1981). We show that the broken ring of high column density neutral hydrogen surrounding the center of WLM is likely the result of star formation propagating out from the center of the galaxy. The young stars and Hα emission in this galaxy are mostly correlated with the high column density neutral hydrogen. The gap in the central ring is the result of star formation in that region using up, blowing out, or ionizing all of the neutral hydrogen. Like many late-type galaxies, WLM's velocity field is asymmetric with the approaching (northern) side appearing to be warped and a steeper velocity gradient for the approaching side than for the receding side in the inner region of the galaxy. We derive a dynamical mass for WLM of 2.16×10^9 $M_\odot$.

Subject headings: galaxies: dwarf, galaxies: irregular, galaxies: ISM, galaxies: kinematics and dynamics, Local Group, galaxies: individual (WLM)

1. Introduction

The interstellar medium of dwarf irregular galaxies provides important information about how stars and gas interact in low mass environments. Feedback from massive stars is the dominant process that affects the interstellar medium in these galaxies. Their low mass makes it easier for violent episodes of star formation to disrupt the galaxy's gas, possibly even expelling it from the galaxy's potential (Mac Low & Ferrara 1999). The lack of differential rotation in dwarf irregulars contributes to longer lifetimes for features like holes in the interstellar medium created by star formation. These longer hole lifetimes allow one to probe the interaction of massive stars and the interstellar medium over longer timescales than possible in other types of galaxies.

As part of an ongoing survey of dwarf irregular galaxies with apparently extended neutral hydrogen emission (Wilcots & Hunter 2002; Hunter & Wilcots 2002), we have obtained observations of the neutral hydrogen, ionized hydrogen, and stellar content of an isolated Local Group dwarf irregular galaxy called WLM. Its nearest neighbor, the Cetus dwarf spheroidal galaxy, is approximately 200 kpc away, assuming a distance to Cetus dSph of 775 kpc (Whiting et al. 1999). Half of WLM's stars, by mass, were formed over 9 Gyr ago, and since then it has been forming stars at a leisurely rate of $1 - 2 \times 10^{-4}$ $M_\odot$ yr^{-1} (Dolphin 2000). In the last Gyr or so, there has been a spurt of star formation, with new stars being formed at three times the average rate in the past (Dolphin 2000). Youngblood & Hunter (1999) identified 30 Hα regions in WLM, which is consistent with its recent spurt of star formation. Like many dwarf irregulars, WLM has a low metallicity; its oxygen abundance is $12 + \log \mathrm{O/H} = 7.78$–$8.23$ (Skillman et al. 1989; Hunter & Hoffman 1999), where 8.7 is solar. Given its metallicity, it is not surprising that Taylor & Klein (2001) did not detect any CO emission in this galaxy, since the CO to H_2 ratio is thought to decrease significantly for low metallicity galaxies. WLM also has a globular cluster with an age of 14.8 ± 0.6 Gyr on its western edge (Hodge et al. 1999), which is very unusual for a faint dwarf irregular (Billett et al. 2002).

We present the highest spatial resolution study to date of the neutral hydrogen content of WLM. Previous studies include Jackson et al. (2004) (spatial resolution: $39''$ by $161''$; velocity resolution: 1.65 km s^{-1}), Barnes & de Blok (2004) (spatial resolution: $15.5'$; velocity resolution: 1.12 km s^{-1}), and Huchtmeier et al. (1981) (spatial resolution: $9'$; velocity resolution: 11 km s^{-1}). WLM's declination makes it difficult to observe; it is low enough in the sky for Very Large Array's (VLA) beam to be elongated and is too near the celestial equator to get good uv coverage with the Australia Telescope Compact Array (ATCA). We have obtained VLA[1] observations of WLM in the B, C, and D configurations. Although our beam is elongated in the north-south direction due to the low declination, the high spatial resolution of these observations allows us to investigate in detail the HI content of this galaxy. We have complemented these observations with UBV and Hα imaging to gain a more complete picture of the interaction between the stars and the interstellar medium in WLM. Our data are discussed further in Section 2. In Section 3, we use our data to examine the properties of the total HI content of WLM. We examine the connection between the small-scale structure of WLM's interstellar medium and its stars in Section 4. Section 5 is a detailed look at the rotation curve of WLM (associated mass modeling is shown in Appendix A). Our conclusions are summarized in Section 6.

2. Data

2.1. VLA observations

Previous observations of WLM (Huchtmeier et al. 1981) indicated that the HI extent of WLM is larger than the primary beam of the VLA at 20 cm ($45'$ versus $30'$), so we mapped WLM in D array as a 3 by 3 mosaic with pointing centers $15'$ apart to make sure that we would detect the total extent of the large scale structure. The resulting square field of view is $60'$ (at the half-power points). These observations were taken on 2001 October 19. The data were on-line hanning smoothed to give a final channel width of 2.57 km s^{-1} . The flux calibrator (0137+331) was observed at the beginning and end of the observations. During the observations, we cycled through the mosaic positions, observing each for 100 s per cycle. We observed the phase calibrator (2321-163) once every two cycles through the mosaic. The total integration time for each pointing was 28 minutes. The effective total integration time for positions near the center of the mosaic was between 128 and 140 minutes due to the overlap between the pointings.

To obtain information on the small scale HI structure of WLM, we observed it using the VLA in B and C configurations. The B array observations were taken on 2002 July 9 and 12 and consisted of a single pointing centered on WLM's position. The flux calibrator (0137+331) was observed for 15 minutes at the end of each day and the phase calibrator

[1]The VLA is part of the National Radio Astronomy Observatory, which is a facility of the National Science Foundation operated under cooperative agreement by Associated Universities, Inc.

(2357-114) was observed for 5 minutes after every 30 minutes of time on source. The total on-source integration time for WLM in B array was 8.5 hours. The C array observations were taken on 2000 March 31 and consisted of a single pointing centered on WLM's position. The flux calibrator (0137+331) was observed for 20 minutes in the middle of the observations and the phase calibrator (2321-163) was observed for 5 minutes after every 35 minutes on source. The total on-source integration time was 5.1 hours. The correlator setup for both the B and C array observations was identical to the D array observations; the final channel width was 2.57 km s^{-1} .

The observations are summarized in Table 1. Data from each day and each array configuration were calibrated separately in AIPS using the standard calibration procedure outlined in the AIPS Cookbook (Greisen 2002). After calibration, the data were imported into Miriad (Sault et al. 1995) for further flagging as well as continuum subtraction, imaging, mosaicking, and cleaning.

From these data, we produced three final data cubes: two from the D-array mosaic and one from the central pointing of the D array mosaic plus the B and C array observations (hereafter, the B+C+D array cube). Table 2 gives the final noise and beam size in all three cubes. We use the D array mosaic observations to investigate the large scale structure and total extent of WLM. After making an initial image to determine the line-free channels, the continuum was subtracted from the initial pointings using the task *uvlin*. Then the nine pointings were put together using the mosaic option in the *invert* task. Two different weightings were used: robust equal to 5 (natural weighting) and robust equal to -5 (uniform weighting). The resulting data cubes were then cleaned using the *mossdi* task to deconvolve the source distribution from the antenna sampling pattern. Images were cleaned to the 2σ noise level and the main emission region was selected. Both the MEM and Clean algorithms yielded similar results for these observations. The Clean algorithm results were used since the final cube had fewer image artifacts after deconvolution. Channel maps for this cube are given in Figure 1 and the total intensity (moment zero) image is shown in Figure 2.

We used the B+C+D array cube to investigate the small scale HI structure of WLM. The observations from the B and C configurations were imaged separately using the *invert* task to make sure there were no problems with the data from individual configurations. After flagging, the uv data sets for each array configuration were combined with *uvcat*. The resulting data set was continuum subtracted (*uvlin*), imaged (*invert*), and cleaned to the 2σ noise limit (*clean* with Miriad choosing the best cleaning algorithm and the main emission region selected). The final map was produced using robust equal to zero because this value yielded the best beam profile; other values yielded non-Gaussian beam profiles. Figure 3 gives channel maps for this data cube. Figures 4, 5, and 6 show the total intensity (moment zero) image, the mean velocity (moment one) image, and the velocity dispersion (moment two) image for this data cube.

The moment images were created using the AIPS task MOMNT. We smoothed the cubes to three times the resolution in the RA, Dec, and velocity directions. The smoothed cube was blanked below the 3σ noise limit and used as a mask for unsmoothed cube. The channels of the masked, unsmoothed cube are then combined to create a moment zero, one, or two image of the data.

We did not use the combination of the D array mosaic with the central B and C array observations in our analysis because the beam (and the noise) would vary significantly across the image greatly complicating analysis. A test image created in Miriad combining the D array mosaic with the B and C observations does not reveal any new galaxy features that are not apparent in the two cubes described above.

2.2. Optical Images

Hα images of WLM were obtained using the Perkins 1.8 m telescope at Lowell Observatory in 1992 November. The observations used an 800×800 TI CCD provided to Lowell Observatory by the National Science Foundation, the Ohio State University Fabry-Perot that was used as a 3:1 focal reducer, an Hα filter with a FWHM of 32 Å, and an off-band filter centered at 6440 Å with a FWHM of 95 Å. The off-band filter was used to subtract stellar continuum from the Hα filter to leave only the Hα nebular emission. In order to survey the entire galaxy, two separate pointings were mosaicked to produce the final Hα image. The exposure times were 3000 s. The pixel scale was $0.49''$, and the seeing was $\sim 2.5''$. Additional details can be found in Hunter & Elmegreen (2004).

UBV images of WLM were obtained using a SITe 2048×2048 CCD on the Hall 1.1 m telescope at Lowell Observatory in three observing runs during 1998 October, 1999 October, and 2002 November. The exposures were 3×1200 s in V, 4×2400 s in B, and 6×2400 s in U. The seeing was about $3.0''$, and the pixel scale was $1.13''$. The telescope position was offset between each image in order to allow removal of cosmic rays. The bias was subtracted using the overscan strip, and the images were flat-fielded using observations of twilight sky. Landolt (1992) standard stars were used to calibrate the photometry. Additional details can be found in Hunter & Elmegreen (2006).

3. HI Mass and Extent

We obtained a total HI flux for WLM of 294 ± 15 Jy km s^{-1} by integrating the HI spectrum from the naturally weighted D array mosaic cube. See Figure 7 for the spectrum. This HI flux corresponds to an HI mass of $6.3 \pm 0.3 \times 10^7$ M$_\odot$ at distance of 0.950 Mpc (Dolphin 2000). Our flux agrees well with the Parkes Multibeam observations of Barnes & de Blok (2004), which give a total HI flux of 292^{+25}_{-15} Jy km s^{-1} . Therefore, our interferometric observations have recovered most of the HI flux in WLM. Jackson et al. (2004) obtained an integrated flux density for WLM of only 149 Jy km s^{-1} from their Australia Telescope Compact Array (ATCA) observations, which lack the short spacings needed to recover extended emission.

To compare our naturally weighted, D-array integrated intensity map (Figure 2) with the single dish maps of Barnes & de Blok (2004) and Huchtmeier et al. (1981), we smoothed the D array cube to the same spatial resolution as Barnes & de Blok (2004, 14.4′) and Huchtmeier et al. (1981, 9′) and created moment maps from the smoothed cubes. Our smoothed maps reach similar noise levels to both Barnes & de Blok (2004) and Huchtmeier et al. (1981). We see that our map agrees well with that of Barnes & de Blok (2004). We do not, however, see the irregular, low surface brightness features observed by Huchtmeier et al. (1981). Huchtmeier et al. (1981) note that they were not able to separate emission from WLM from the nearby Magellanic Stream emission because of their low velocity resolution (11 km s^{-1}); the tail of the Magellanic Stream is very close to the position of WLM at an LSR velocity of –200 km s^{-1} (Putman et al. 2003). Huchtmeier et al. (1981) estimated the mass of WLM by assuming symmetry in WLM's line profile. Although Barnes & de Blok (2004)'s spatial resolution is larger (14.4′ vs. 9′), their superb velocity resolution (1.12 km s^{-1} , a factor of 10 lower than that of Huchtmeier et al.) allows one to easily separate WLM's emission from that of the Magellanic Stream in most channels. We, fortunately, resolve out the Magellanic Stream. Given the line profiles shown in Figure 7 and in Barnes & de Blok (2004), it is clear that WLM's line profile is not symmetric and that Huchtmeier et al. (1981)'s integrated HI mass and maps for this galaxy are not accurate.

WLM's HI only extends to 1.2 times its Holmberg diameter, not the 3.6 times found by Huchtmeier et al. (1981). We find that the HI diameters quoted for other galaxies in the Huchtmeier et al. (1981) sample are also too large. Deep neutral hydrogen observations of Sextans A with the Green Bank Telescope (Bowsher et al. 2003) do not detect the extended gas reported by Huchtmeier et al. (1981) confirming the results of VLA D-array observations reported by Wilcots & Hunter (2002). VLA D-array mosaic observations of NGC 2366 reduced by Wilcots also do not show signs of the extended HI reported by Huchtmeier et al. (1981).

Figure 8 gives the surface density profile for WLM. The inclination and position angle of the galaxy were taken from the naturally weighted D array rotation curve (see Section 5) and the disk scale length (R_D=2.0′) from Hunter & Elmegreen (2006). Comparing the surface density profile of WLM to the surface density profiles of the other dwarf galaxies in Figure 8, we see WLM's HI distribution is typical of a dwarf irregular galaxy. Several other galaxies in this Figure (NGC 2366, NGC 4449, IC 1613, Sextans A, and DDO 88) have central HI depressions like WLM's. From Figure 8, one can see that the average surface density of WLM's ring is about 1.3 times that of the center. The contrast increases to 1.4 times that of the center in the portion of the ring with the highest surface density. This ratio is smaller than the ratios between ring surface density and central surface density seen in galaxies like Sextans A ($\sim$ 1.8) and DDO 88 ($\sim$ 2) and is more like the ratio seen in DDO 105 ($\sim$ 1.2). WLM's peak surface density (7.5 $M_{\odot}$ pc^{-2}) is average for galaxies in this sample. Its HI extends to 8.5 times the optical disk scale length; six of the ten galaxies in Figure 8 have larger HI extents.

4. Small Scale HI Structure

From Figure 4, we can see that the neutral hydrogen distribution of WLM is smooth with a large central depression and slightly asymmetric. Comparing our Figures 2 and 4 to Figure 4 in Jackson et al. (2004) illustrates why it is crucial to have good uv plane coverage for a detailed examination of the HI structure of a galaxy. What we were able to image as a broken ring of high column density HI surrounding the center of the galaxy, Jackson et al. (2004) was only able to image as two asymmetric high column density peaks. We refer to the broken ring of high column density HI as the "hook": the handle of the hook is the high column density HI extending northward and the hook itself extends from the handle south and east around the ring until it ends at the southernmost bit of high column density gas. Approximately 20% of the total mass of WLM is in the hook. From the first moment image (Figure 5), which shows the velocity centroid distribution, and the position-velocity diagram (Figure 13), one can see that the velocity distribution is asymmetric (see Section 5 for details). The second moment image in Figure 6 is also asymmetric, with the northern half of the galaxy having a higher average velocity dispersion than the southern half. Note that the maximum velocity dispersion is approximately 10 km s^{-1} and the average velocity dispersion for the entire galaxy is 4.5 km s^{-1} . We do not see any sign of the hook expanding; plots of spectra in the region as a function of position are single-peaked.

How does WLM's neutral hydrogen distribution compare to its stellar and ionized hydrogen distributions? Figure 9 shows a color image of the optical data described in Section 2.2

with HI contours overlaid. The distribution of the blue stars is closely correlated with the high column density HI with the exception of the clump of blue stars on the western edge of the galaxy. The HI hook is also well correlated with the Hα emission (see Figure 10) except for the C2 complex in the southwestern portion of the galaxy. This bubble-like Hα region corresponds to an HI *deficit* at the center of the bubble. Finally, there is faint, diffuse Hα emission along the inner eastern edge of the hook indicating that there is on-going star formation in this region.

HI deficits in the center of dwarf irregulars are fairly common (see Figure 8). These rings are thought to be formed by the stellar winds and supernova explosions of high mass stars (McCray & Kafatos 1987; Elmegreen 1994). The high mass stars clear out a bubble in the interstellar medium which continues to expand until its expansion velocity slows to the velocity dispersion of the galaxy. Gas piles up on the edge of the bubble and can, in turn, form more stars. There is, however, little definitive observational evidence that this process is what creates HI rings. Ott et al. (2001) find evidence that the central ring in Holmberg I was the result of a blowout. They find an age for the HI ring that matches the age of the stellar populations inside it. Associated hydrodynamic simulations by Vorobyov et al. (2004) show that multiple supernovae can produce a feature like the ring seen in Ho I. HST/ACS observations by Momany et al. (2005) of the stellar populations of a portion of SagDIG, however, indicate that there were not enough stars formed in the central region of the galaxy to generate the observed HI ring. In their study of DDO 88, Simpson et al. (2005a) find that while the star cluster in the center of the galaxy had enough mass to form the HI ring seen today, the cluster is too old and that any HI ring formed by a population as old as the cluster would have dissipated by the present day. Is the hole in the center of WLM the result of multiple supernova explosions? We can use our observations of WLM's neutral hydrogen along with the star formation properties of WLM (Dolphin 2000) to test this hypothesis.

The first quantity we need to estimate is the timescale for the formation of the hook. Assuming that the hook resulted from an expanding shell, we can place a rough upper limit on its age. The average central velocity dispersion of WLM is approximately the final expansion velocity of the ring if the ring is stalled. Using this velocity (7 km s^{-1}) and the radius of the hook (R_{inner} = 250 pc; R_{outer} = 462 pc), we obtain an upper limit on the expansion time of the ring between 35 Myr (using the inner radius of the ring) and 69 Myr (using the outer radius of the ring). An upper limit on the dispersion time for the ring can be estimated by finding the time it would take for the ring to expand to twice its observed width. Using the same velocity dispersion as above, this time scale is approximately 59 Myr. Therefore, the upper limit on the age for WLM's hook (expansion time plus dispersion time) is between 94 and 128 Myr.

We can use models of a supernova explosion in a uniform medium (Chevalier 1974) to estimate the energy needed to create WLM's HI hole. To do this, we must first estimate the number density of HI at mid-plane (n_0). Using an inclination of 75° for WLM and a scale height typical of a dwarf irregular galaxy (500 pc), we obtain a pathlength through the galaxy of 3800 pc. Dividing the central surface density (1.96×10^{21} cm^{-2}) by this pathlength gives an estimate of n_0 of 0.16 cm^{-3}. A reasonable upper limit on n_0 is 1 cm^{-3} given the properties of HI in other galaxies. Equation (26) of Chevalier (1974) gives an estimate of the supernova energy needed to produce a hole of radius R from an explosion into a medium of uniform density n_0. For WLM's HI hole, the total HI kinetic energy is between 3.1×10^{51} erg and 2.45×10^{52} erg, which corresponds to between 3 and 24 supernovae.

Has WLM formed enough stars during the last 94 to 128 Myr to produce that many supernovae? Although there have been several stellar population studies of WLM (Ferraro et al. 1989; Minniti & Zijlstra 1997; Rejkuba et al. 2000; Dolphin 2000), there are no spatially resolved star formation histories for the entire galaxy. The highest resolution stellar population study was done by Dolphin (2000), who used WFPC2 on Hubble Space Telescope (HST) to get a detailed star formation history for three regions in the western half of the galaxy. Figure 11 shows the location of his fields.[2] Unfortunately, his observations missed the high column density HI regions, both large HII regions in the galaxy (Hodge & Miller (1995)'s C1 and C2 complexes), and the region of blue stars uncorrelated with the hook. In his relatively quiescent survey region, he finds that 85% of WLM's star formation in the past 200 Myr is in the region surveyed that was closest to the center of the galaxy and that the galaxy has been experiencing a burst of star formation in the past Gyr.

We can see if WLM has had enough recent star formation to form its HI hole. Using a typical star formation rate for WLM (1.0×10^{-4} M$_\odot$ yr^{-1}) scaled to the area interior to the ring (1.6×10^{-4} M$_\odot$ yr^{-1}) and the maximum lifetime time for the bubble, we derive a total mass of stars formed between 1.5×10^4 M$_\odot$ and 2.1×10^4 M$_\odot$. Using a Salpeter initial mass function (Salpeter 1955), we find that during the lifetime of the bubble between 138 and 188 stars were formed with masses greater than 7 M$_\odot$, which exceeds the estimated number of supernovae needed to form the hole. Therefore, it is plausible that the HI hole in WLM was caused by star formation in the center of the galaxy.

Unlike DDO 88's unbroken ring, WLM's HI ring has a significant gap on the western edge of the galaxy and a high column density region extending north along the major axis of the disk. The handle of the hook is probably due to an increase in column density because

[2]The caption of Figure 1 in Dolphin (2000) is incorrect. The WF2 chip is on the upper left, WF3 is on the lower left, and WF4 is on the lower right.

we are looking through the disk of WLM. The origin of the gap in WLM's HI ring is more of a mystery. There are bright, blue stars seen near the C2 Hα complex at the tip of the HI hook, which indicates that in the past there was more neutral hydrogen in this region than is currently seen. It is likely that the star formation in the C2 Hα region has either used up, blown out, or ionized all of the neutral hydrogen. Examining spectra as a function of position in the C2 region at the tip of the HI hook, we see double peaked velocity profiles characteristic of expanding bubbles with the central channel of the profile being lower than the two neighboring channels (see Figure 12). The separation between the two peaks is approximately 9 km s^{-1} , which means that the expansion velocity of the bubble is about 4.5 km s^{-1} . This velocity is very similar to the velocity dispersion of the galaxy as a whole, suggesting that the bubble is near the end of its expansion. The Hα emission in this region also exhibits signs of expansion (Tomita et al. 1998, their Figure 5, slit position WLM E). In contrast to the C2 region, the current round of star formation in the HI hook (indicated by the faint Hα emission along the inner edge of the hook), however, seems to be just beginning and it has yet to deplete the neutral hydrogen in this region. The higher velocity dispersion in the northern half of the galaxy reflects the disruption of the ISM by the star formation taking place in the northern half of the galaxy. A detailed, spatially resolved star formation history of the entire galaxy is needed before we can attempt to conclusively correlate neutral hydrogen features with star formation episodes.

Minniti & Zijlstra (1997) have suggested, based on a paper by Wallin et al. (1996), that WLM's globular cluster may have triggered the recent star formation episode in this galaxy a Gyr ago. Although we believe that this possibility is unlikely, the globular cluster in WLM, assuming a typical globular cluster mass of 10^6 M$_\odot$ and a typical WLM halo velocity of about 40 km s^{-1} , does have a total kinetic energy of 1.6×10^{52}erg. If a tenth of this energy was transferred to WLM, this energy input would be similar to the energy input by one supernova. Without full orbital parameters for the globular cluster, we cannot exclude the possibility that a particularly close/violent encounter between WLM and its globular cluster has triggered the latest round of star formation.

Another scenario is that a close encounter with the nearby Cetus dwarf spheroidal galaxy may have triggered the star formation. Unfortunately, in this case, we are again without detailed orbital parameters. We can constrain the time since interaction, however, by assuming that WLM and Cetus dSph are on radial orbits. Then the time since interaction is just the distance between the two galaxies (200 kpc) divided by the velocity dispersion of the Local Group (~ 60 km s^{-1} ; van den Bergh 1999), which yields a time of 3.4 Gyr. This time is same order of magnitude as the start of the latest burst of star formation in WLM a Gyr ago (Dolphin 2000).

Bars can also create a central HI deficit (e.g. Ryder et al. 1996). However, we see no evidence for a bar in a Spitzer IRAC 3.6 μm image of the central portion of WLM. While the approaching side of WLM is clearly warped, we do not see any s-shaped isovelocity contours in the center of the galaxy that are indicative of a bar (e.g. Ryder et al. 1996, NGC 1433).

5. Rotation Curve

The position-velocity plot of the B+C+D array data cube in Figure 13 provides a first look at the rotation curve of WLM. This plot shows the velocity distribution as a function of position along a slice corresponding to the major axis of WLM's neutral hydrogen distribution. There are several things to notice about this graph. First, WLM is clearly rotating with a velocity of approximately 30 km s^{-1} . Second, the rotation curve is not symmetric. The rotation curve for the approaching side of the galaxy increases to a velocity of 30 km s^{-1} then levels off; the rotation curve for the receding side of the galaxy rises much more slowly, does not level off and is slightly distorted at the location of the ring. Finally, the ring seen in Figure 4 is clearly visible in this plot as the two dark spots at $\pm 1.5'$.

To derive a rotation curve for the entire galaxy, we fit a tilted ring model to the velocity field of the B+C+D array cube. Tilted ring models divide the galaxy into a series of annuli and determine the position angle, inclination, and rotation velocity independently for each ring. See Begeman (1987) for more detailed information about this type of model. The small beam size of the B+C+D array cube allows us to finely sample the rotation curve and minimize beam smearing effects. Initial guesses for the fit parameters were taken from the literature. We refined these guesses by fitting functions to the velocity field. To determine the center of the galaxy and an approximate inclination, we fit a Brandt type rotation curve to WLM's velocity field using the *GAL* task in AIPS. Then we fit a solid body rotation curve to the velocity field to determine the systematic velocity and get a good estimate of the position angle. Note that we could not use just one function to get all five initial parameters because although the velocity field is better fit by a solid body rotation curve, a solid body rotation curve cannot determine the center of a galaxy. We used the *rotcur* task (Begeman 1987, 1989) in GIPSY (Vogelaar & Terlouw 2001; van der Hulst et al. 1992) to fit a tilted ring model to the velocity field of the galaxy. The width of each annulus was $15''$. The widths of the annuli were chosen to be slightly less than the major axis of our elliptical beam. We started the fits one beam width from the center to avoid beam-smearing effects. We have corrected the errors produced by *rotcur* to take into account that all the pixels in the ring are not independent.

Note that we also fit tilted ring models to the naturally weighted, D array cube velocity fields using the same method. However, since these fits are affected by beam smearing in the inner regions and do not yield new information about the rotation curve of WLM, we do not discuss them here.

For the B+C+D array cube, attempting to fit the inclination, position angle, and rotation velocity with the same parameters for the entire galaxy led to large residuals with spatial structure. Since the approaching (north) and receding (south) halves of WLM are not symmetric, we decided to fit the inclination, position angle, and rotation velocity for each side of the galaxy separately. The resulting fits are shown in Figure 14. The blue and red lines show the fit for approaching and receding sides of the B+C+D array cube, respectively. The weighted average of the fitted inclination and position angle for each model are given by thin solid lines running across the lower two plots.

Examining the top panel of Figure 14, we see that the rotation curve for the approaching half of the B+C+D array data levels off at about $2.5'$ to a value of 30 km s^{-1} , while the rotation curve of the receding half continues to rise. The B+C+D array rotation curves are relatively bumpy because the B+C+D array cube is sampling velocities on size scales of approximately 50 pc, where small scale velocity features from SNe, for example, dominate. (See Section 4 for a discussion of the velocity dispersion distribution of WLM.)

From Figure 14, one can see that the inclination of the galaxy based on the high resolution fits is more or less constant as a function of radius. The weighted average inclination for each fit is given in Table 3. There is an 8° offset in the inclination between the two sides of the galaxy for the B+C+D array rotation curve.

The position angle as a function of radius shows greater variation than the inclination as a function of radius. The position angles of the B+C+D fits change rather abruptly at particular radii. In the fit to the approaching side of the B+C+D array cube, the position angle changes from about 172° to about 178° at $2.5'$, decreases to about 170° at $6.5'$ and then begins to increase again at $8'$. Note that the position angle for radii greater than $9'$ is very uncertain. The fit to the receding side of the B+C+D array cube increases from about 170° to about 180° between a radius of $5'$ and a radius of $8.5'$. The average position angle for the approaching side is 3° higher than the average position angle for the receding side for the high resolution data cube.

The asymmetry in WLM's rotation curve is not unusual; half the dwarf galaxies in the Westerbork HI Survey of Spiral and Irregular Galaxies (WHISP) are kinematically lopsided (Swaters et al. 2002). Only 16% of these galaxies are clearly interacting. Swaters et al. (2002) attributes the rest of the distortions to long-lived remnants of past interactions. WLM has at least two neighbors that are close enough to have disrupted its neutral hydrogen recently:

its ancient globular cluster and the Cetus dwarf spheroidal ($\sim$ 200 kpc away). See Section 4 for a discussion of the interaction of WLM with these objects. The presence of a globular cluster suggests that WLM interacted with something a long time ago; many of the dwarfs that have young super star clusters in them today have nearby HI clouds or show other signs of an interaction (Billett et al. 2002).

We can use our derived rotation curves to fit a mass model to the data and determine the dynamical mass of WLM. The details of this procedure are in Appendix A. We derive a dynamical mass of 2.16×10^9 $M_\odot$ for WLM. Our mass models show that WLM is extremely dark matter dominated when compared to the dwarf irregular galaxies in Côté et al. (2000).

Jackson et al. (2004) derived a rotation curve for WLM from their low resolution HI data. Their rotation curve (see Jackson et al. 2004, Figure 8) is very similar to our curve (see our Figure 14). It reaches a velocity of about 38 km s^{-1} at a radius of 4 kpc, while our low resolution curve reaches a velocity of about 42 km s^{-1} at the same radius. We also derive similar halo dynamical masses.[3]

6. Summary and Conclusions

Dwarf irregular galaxies are unique laboratories for studying the interaction between stars and the interstellar medium in low mass environments. In this paper, we have presented the highest spatial resolution observations to date of the neutral hydrogen content of the Local Group dwarf irregular galaxy WLM. These observations have allowed us to study the interstellar medium of WLM in detail. The major conclusions of this work are:

- WLM's neutral hydrogen distribution is typical for a galaxy of its type and size. Our synthesis observations were able to recover all of the HI flux from this galaxy; we derive an HI mass of $6.3 \pm 0.3 \times 10^7$ $M_\odot$ for WLM. We derive an HI extent of $\sim 30'$, which is much less than the $45'$ extent derived by Huchtmeier et al. (1981). In the central region of WLM, the HI has a hook-like distribution, i.e., a central broken ring of HI with a linear feature extending northwards from the top of the broken ring.
- We shoe that the hook is likely the result of star formation propagating out from the center of the galaxy. The young stars and Hα emission in this galaxy are mostly spatially correlated with the neutral hydrogen peaks. The gap on the western edge of

[3]Note that the dynamical mass quoted in Jackson et al. (2004) is incorrect. According to D. Jackson (2006, private communication), the correct dynamical mass is 1.4×10^9 $M_\odot$.

the hook is likely the result of star formation in that region using up, blowing out, or ionizing all of the neutral hydrogen. The diffuse Hα on the eastern edge of the hook indicates that there is ongoing star formation in the central region of WLM.

- WLM's velocity field is asymmetric. The approaching (northern half) appears to be warped and the inner approaching region has a steeper velocity gradient than the inner receding region. We derive a dynamical mass for WLM of 2.16×10^9 M$_\odot$.

In short, WLM is a typical dwarf irregular galaxy undergoing a recent burst of propagating star formation that is disrupting its neutral hydrogen. A detailed, spatially resolved star formation history of the entire galaxy would allow us to track the progress of the star formation across the galaxy and attempt to correlate particular HI features with specific episodes of star formation.

A. A. K. was supported by a National Science Foundation Graduate Research Fellowship and a Wisconsin Space Grant Consortium Graduate Fellowship during portions of this work. E. M. W. gratefully acknowledges the support of NSF grant AST-0098438. Funding for this work was provided to D. A. H. by the Lowell Research Fund and the NSF through grant AST 02-04922. The authors would also like to thank E. Brinks, B. Elmegreen, D. Westpfahl, V. McIntyre, and G. Ostlin for their work on the proposal for these observations. A. A. K. would like to thank Marc Verheijen and Linda Sparke for helpful conversations and Erwin de Blok for providing us with his WLM data cube.

Facilities: VLA, Hall, Perkins

A. Deriving the Dynamical Mass of WLM

We can use our derived rotation curves to fit a mass model to the data and determine the dynamical mass of WLM. There are a variety of techniques and subtleties associated with fitting mass models (see Swaters et al. (2000); de Blok et al. (2001a,b); van den Bosch & Swaters (2001); de Blok & Bosma (2002); de Blok et al. (2003); McGaugh et al. (2003); Swaters et al. (2003a,b); Weldrake et al. (2003); de Blok (2005); Gentile et al. (2005) for a sampling). Here we outline our procedure.

For each side of WLM, we used a combination of the B+C+D array and the D array mosaic rotation curves to fit a mass model. The D array mosaic rotation curves were generated the same way as the B+C+D array rotation curves (see Section 5). The D array mosaic rotation curve extends to larger radii than the B+C+D array rotation curve, which is crucial for constraining the halo model. The B+C+D array rotation curve is less affected by beam smearing in the inner regions than the D array mosaic rotation curve, so it is better at constraining the disk model. We spliced the B+C+D rotation curve to the D array mosaic curve at $9'$ for the approaching side and at $5'$ for the receding side. The B+C+D array and the D array mosaic rotation curves agree in the overlap region.

We used a simple model consisting of a gas disk, a stellar disk, and a halo to determine the dynamical mass of WLM. For the gas disk, we found the neutral hydrogen contribution to the total rotation curve from the HI surface density profile, whose inclination and position angle were fixed to the appropriate values for the B+C+D array data, using the method of Begeman (1987) and Casertano (1983). The square of the rotation velocity of this component (which is proportional to the HI mass distribution) was then multiplied by 1.43 to account for the presence of helium and other gas. The contribution of the optical component to the total rotation curve was found from a V-band surface brightness profile (Hunter & Elmegreen 2006) using the same method. We converted the luminosity distribution of the galaxy into a mass distribution (which is proportional to the rotation velocity squared) by multiplying the luminosity distribution by a mass-to-light ratio. The mass-to-light ratio is a free parameter in our fits. It was restricted to physically meaningful values, i.e., the mass-to-light ratio had to be greater than zero. We also assumed that the mass-to-light ratio did not change as a function of radius in the galaxy. For the halo, we used two different models: an isothermal sphere and a NFW halo (Navarro et al. 1997). The first model is generally a good fit to the data and the second model is suggested by cosmological simulations. The circular velocity for the isothermal sphere with density distribution

$$\rho(r) = \rho_0 \left[1 + (r/a)^2\right]^{-1} \tag{A1}$$

is given by

$$v_{c,iso}(r)^2 = 4\pi G \rho_0 a^2 [1 - (a/r)\arctan(r/a)], \tag{A2}$$

where ρ is the density, r is the radius, ρ_0 is the central halo density, and a is the core radius (e.g. McGaugh & de Blok 1998). For the NFW halo, the circular velocity is given by

$$v_{c,nfw}^2 = \frac{v_{200}^2}{x} \frac{\ln(1+cx) - cx/(1+cx)}{\ln(1+c) - c/(1+c)} \tag{A3}$$

where r_{200} is the radius where the overdensity is 200 times that of the background density, v_{200} is the velocity at r_{200}, x is r/r_{200}, and c is the concentration parameter. The parameters r_{200} and v_{200} are related by the equation

$$v_{200} = \left(\frac{GM}{r_{200}}\right)^{1/2} = \left(\frac{r_{200}}{h^{-1}\ \mathrm{kpc}}\right) \left[\frac{\Omega_0}{\Omega(z_0)}\right]^{1/2} (1+z_0)^{3/2}\ \mathrm{km\ s^{-1}} \tag{A4}$$

where Ω_0 is the current matter density and $\Omega(z_0)$ is the matter density at redshift z_0. The redshift of WLM was taken to be 0. The concentration parameter is just r_{200} divided by the scale radius of the halo so it was restricted to be greater than or equal to one ($r_{200} \geq r_s$).

We fit three different types of mass models to the data: a maximum disk model, a maximum halo model, and a best fit mass model. The maximum disk model fits the data assuming a maximal contribution from the disk to the rotation curve. Note that this mass model still includes a halo component to the fit since a disk rotation curve cannot replicate the flat portion of the observed rotation curve. The maximum halo model fits the data assuming that there is no contribution to the rotation curve from the stellar or gas disk. These two fits, while clearly not physical, provide important boundary conditions for our mass model of WLM. The best fit mass model is a model of the galaxy which includes contributions from the halo, the stellar disk, and the gas disk. For this fit, the parameters for each component of the mass model are chosen to minimize the difference between the observed and the model rotation curves using the χ^2 parameter as our minimization criterion. We used the downhill simplex (amoeba) method of Nelder and Mead (Press et al. 1992) to find the mass model parameters which minimized the χ^2 value. While this might not be the best algorithm for minimizing the χ^2 parameter, it does have the advantage of being easy to implement and relatively fast given that we only had to fit three parameters. To ensure that the algorithm found a truly global minimum, we ran it with a grid of different initial guesses for the parameters and chose the solution that had the lowest chi-squared value. See Tables 4 and 5 for a summary of the mass model fits and Figure 15 for plots of the best fit mass models.

We were not able to generate an acceptable mass model fit to the entire rotation curve for the approaching side. The rotation curve for the approaching side (see the plots on the left hand side of Figure 15) increases rapidly at radii greater than $8'$, deviating from the behavior of a well-behaved rotation curve (cf. the rotation curve for the receding side of the galaxy in show in the plots on the right hand side of Figure 15). The warp can also be seen in Figure 5. The isovelocity contours form a U-shape on the northern (approaching) side of the galaxy, while the contours on the southern (receding) side remain more or less straight. Unfortunately, there is not enough information in either the B+C+D rotation curve or the D array mosaic rotation curve to constrain the change in inclination and/or position angle. However, the unusual rotation curve generated for the approaching side obtained by fixing both the inclination and position angle to a single set of values points to unconstrained variations in the inclination and position angle. Since the approaching side of the galaxy is affected by a warp at radii greater than $8'$, we excluded these radii from our fit. Note that the results in Tables 4 and 5 for the approaching side only go out to the last point we fitted.

Due to the apparent warp in the approaching side of WLM, we used the isothermal sphere best fit mass model to the receding side of the galaxy to determine an estimate for the dynamical mass of the galaxy (2.16×10^9 $M_\odot$) and the mass model parameters for the entire galaxy. The maximum halo model (no disk) for the receding side yields a relatively good fit to the data for the isothermal sphere case. The maximum disk model, however, yields poor χ_r^2 values for all fits. WLM is clearly not a galaxy whose dynamics are dominated by its disk. Note that WLM's estimated total dynamical mass changes by less than 10% between the isothermal sphere halo and the NFW halo best fits for the undisturbed receding side of the galaxy.

We also compared our best fit mass model (isothermal sphere halo plus gas and stellar disks) parameters for WLM with those derived for a sample of five dwarf irregular galaxies by Côté et al. (2000). We find that the core radius and central density for the receding side of the rotation curve as well as the derived galaxy parameters (stellar M/L ratio, total dynamical mass, and ratio of mass in dark matter to the mass in luminous matter) are within the range of values established by these authors. The halo parameters for the approaching side of the galaxy fall outside the Côté et al. distribution, but these parameters are not well constrained for the the approaching side because of the warp. WLM, when compared with the galaxies in the Côté et al. sample, is on the extremely dark matter-dominated end of the dwarf galaxy spectrum.

REFERENCES

Barnes, D. G., & de Blok, W. J. G. 2004, MNRAS, 351, 333

Begeman, K. G. 1987, Ph.D. Thesis

—. 1989, A&A, 223, 47

Billett, O. H., Hunter, D. A., & Elmegreen, B. G. 2002, AJ, 123, 1454

Bonnarel, F., Fernique, P., Bienaymé, O., Egret, D., Genova, F., Louys, M., Ochsenbein, F., Wenger, M., & Bartlett, J. G. 2000, A&AS, 143, 33

Bowsher, E., Hunter, D., Wilcots, E., Kepley, A., & Goad, V. 2003, American Astronomical Society Meeting Abstracts, 203, 115.14

Broeils, A. H. 1992, Ph.D. Thesis

Carignan, C., & Beaulieu, S. 1989, ApJ, 347, 760

Casertano, S. 1983, MNRAS, 203, 735

Chevalier, R. A. 1974, ApJ, 188, 501

Côté, S., Carignan, C., & Freeman, K. C. 2000, AJ, 120, 3027

de Blok, W. J. G. 2005, ApJ, 634, 227

de Blok, W. J. G., & Bosma, A. 2002, A&A, 385, 816

de Blok, W. J. G., Bosma, A., & McGaugh, S. 2003, MNRAS, 340, 657

de Blok, W. J. G., McGaugh, S. S., Bosma, A., & Rubin, V. C. 2001a, ApJ, 552, L23

de Blok, W. J. G., McGaugh, S. S., & Rubin, V. C. 2001b, AJ, 122, 2396

Dolphin, A. E. 2000, ApJ, 531, 804

Elmegreen, B. G. 1994, ApJ, 427, 384

Ferraro, F. R., Fusi Pecci, F., Tosi, M., & Buonanno, R. 1989, MNRAS, 241, 433

Gentile, G., Burkert, A., Salucci, P., Klein, U., & Walter, F. 2005, ApJ, 634, L145

Greisen, E. e. 2002, AIPS Cookbook, National Radio Astronomy Observatory, Charlottesville, VA

Hodge, P., & Miller, B. W. 1995, ApJ, 451, 176

Hodge, P. W., Dolphin, A. E., Smith, T. R., & Mateo, M. 1999, ApJ, 521, 577

Huchtmeier, W. K., Seiradakis, J. H., & Materne, J. 1981, A&A, 102, 134

Hunter, D. A., & Elmegreen, B. G. 2004, AJ, 128, 2170

—. 2006, ApJS, 162, 49

Hunter, D. A., Elmegreen, B. G., & van Woerden, H. 2001, ApJ, 556, 773

Hunter, D. A., & Hoffman, L. 1999, AJ, 117, 2789

Hunter, D. A., van Woerden, H., & Gallagher, J. S. 1999, AJ, 118, 2184

Hunter, D. A., & Wilcots, E. M. 2002, AJ, 123, 2449

Jackson, D. C., Skillman, E. D., Cannon, J. M., & Côté, S. 2004, AJ, 128, 1219

Landolt, A. U. 1992, AJ, 104, 340

Mac Low, M.-M., & Ferrara, A. 1999, ApJ, 513, 142

McCray, R., & Kafatos, M. 1987, ApJ, 317, 190

McGaugh, S. S., Barker, M. K., & de Blok, W. J. G. 2003, ApJ, 584, 566

McGaugh, S. S., & de Blok, W. J. G. 1998, ApJ, 499, 41

Minniti, D., & Zijlstra, A. A. 1997, AJ, 114, 147

Momany, Y., Held, E. V., Saviane, I., Bedin, L. R., Gullieuszik, M., Clemens, M., Rizzi, L., Rich, M. R., & Kuijken, K. 2005, A&A, 439, 111

Navarro, J. F., Frenk, C. S., & White, S. D. M. 1997, ApJ, 490, 493

Ott, J., Walter, F., Brinks, E., Van Dyk, S. D., Dirsch, B., & Klein, U. 2001, AJ, 122, 3070

Press, W. H., Teukolsky, S. A., Vetterling, W. T., & Flannery, B. P. 1992, Numerical recipes in FORTRAN. The art of scientific computing (Cambridge: University Press, 2nd ed.)

Puche, D., Westpfahl, D., Brinks, E., & Roy, J.-R. 1992, AJ, 103, 1841

Putman, M. E., Staveley-Smith, L., Freeman, K. C., Gibson, B. K., & Barnes, D. G. 2003, ApJ, 586, 170

Rejkuba, M., Minniti, D., Gregg, M. D., Zijlstra, A. A., Alonso, M. V., & Goudfrooij, P. 2000, AJ, 120, 801

Ryder, S. D., Buta, R. J., Toledo, H., Shukla, H., Staveley-Smith, L., & Walsh, W. 1996, ApJ, 460, 665

Salpeter, E. E. 1955, ApJ, 121, 161

Sault, R. J., Teuben, P. J., & Wright, M. C. H. 1995, in ASP Conf. Ser. 77: Astronomical Data Analysis Software and Systems IV, 433

Simpson, C. E., Hunter, D. A., & Knezek, P. M. 2005a, AJ, 129, 160

Simpson, C. E., Hunter, D. A., & Nordgren, T. E. 2005b, AJ, 130, 1049

Skillman, E. D., Terlevich, R., & Melnick, J. 1989, MNRAS, 240, 563

Swaters, R. A., Madore, B. F., & Trewhella, M. 2000, ApJ, 531, L107

Swaters, R. A., Madore, B. F., van den Bosch, F. C., & Balcells, M. 2003a, ApJ, 583, 732

Swaters, R. A., van Albada, T. S., van der Hulst, J. M., & Sancisi, R. 2002, A&A, 390, 829

Swaters, R. A., Verheijen, M. A. W., Bershady, M. A., & Andersen, D. R. 2003b, ApJ, 587, L19

Taylor, C. L., & Klein, U. 2001, A&A, 366, 811

Tomita, A., Ohta, K., Nakanishi, K., Takeuchi, T. T., & Saito, M. 1998, AJ, 116, 131

van den Bergh, S. 1999, A&A Rev., 9, 273

van den Bosch, F. C., & Swaters, R. A. 2001, MNRAS, 325, 1017

van der Hulst, J. M., Terlouw, J. P., Begeman, K. G., Zwitser, W., & Roelfsema, P. R. 1992, in ASP Conf. Ser. 25: Astronomical Data Analysis Software and Systems I, 131

Vogelaar, M. G. R., & Terlouw, J. P. 2001, in ASP Conf. Ser. 238: Astronomical Data Analysis Software and Systems X, 358

Vorobyov, E. I., Klein, U., Shchekinov, Y. A., & Ott, J. 2004, A&A, 413, 939

Wallin, J. F., Higdon, J. L., & Staveley-Smith, L. 1996, ApJ, 459, 555

Weldrake, D. T. F., de Blok, W. J. G., & Walter, F. 2003, MNRAS, 340, 12

Whiting, A. B., Hau, G. K. T., & Irwin, M. 1999, AJ, 118, 2767

Wilcots, E. M., & Hunter, D. A. 2002, AJ, 123, 1476

Youngblood, A. J., & Hunter, D. A. 1999, ApJ, 519, 55

Table 1. Summary of Observations

Array Configuration	B	C	D
Date	2002 July 9 and 12	2000 March 31	2001 October 19
Number of Pointings	1	1	9
Square Field of View (′)	30	30	60
Channel Width (km s^{-1})	2.57	2.57	2.57
Flux Calibrator	0137+331	0137+331	0137+331
Phase Calibrator	2357-114	2321-163	2321-163
Total Integration Time (hours)	8.5	5.1	∼2

Table 2. Summary of Final Data Cubes

Cube Name	Weighting	Beam Size (″)	1σ Noise per Channel (mJy beam^{-1})	(K)
D array mosaic	Natural	83.84 × 59.11	4.7	0.58
D array mosaic	Uniform	72.77 × 48.88	5.1	0.87
B+C+D array cube	Robust=0	16.17 × 10.59	1.4	5.0

Table 3. Tilted Ring Rotation Curve Fit Results

Data Set	Fit	<P.A.> (°)	$\sigma_{P.A.}$ (°)	<Incl> (°)	σ_{Incl} (°)
D array mosaic	Entire Galaxy	179.3	2.2	69.8	3.7
D array mosaic	Approaching	174.6	2.3	62.8	6.0
D array mosaic	Receding	179.5	2.0	72.2	3.2
B+C+D array	Approaching	175.5	3.8	74.2	3.1
B+C+D array	Receding	172.3	4.1	82.4	5.8

Table 4. Summary of Mass Model Fits with Isothermal Sphere Halos

Fit Type	a ($''$)	ρ_0 ($M_\odot$ pc^{-3})	M/L ($M_\odot$ /$L_\odot$)	χ^2_r	M_{gas} ($M_\odot$)	M_{stars} ($M_\odot$)	M_{halo} ($M_\odot$)
			Approaching Side				
Best Fit	71.5	0.157	0	2.00	6.46×10^7	0	3.82×10^8
Max. Halo	83.3	0.150	$\cdots$	2.57	0	0	4.75×10^8
Max. Disk	0.00985	174000	4.8	9.90	6.46×10^7	2.07×10^8	1.02×10^7
			Receding Side				
Best Fit	337	0.0265	1.1	0.98	9.91×10^7	4.73×10^7	2.01×10^9
Max. Halo	237	0.0483	$\cdots$	0.84	0	0	2.15×10^9
Max. Disk	6870	0.00737	3.6	8.88	9.91×10^7	1.55×10^8	2.64×10^9

Table 5. Summary of Mass Model Fits with NFW Halos

Fit Type	v_{200} (km s^{-1})	c	M/L ($M_\odot$ /$L_\odot$)	χ^2_r	M_{gas} ($M_\odot$)	M_{stars} ($M_\odot$)	M_{halo} ($M_\odot$)
			Approaching Side				
Best Fit	24.6	6.60	0.965	2.34	6.46×10^7	4.17×10^7	3.24×10^8
Max. Halo	32.1	6.81	$\cdots$	5.42	0	0	5.07×10^8
Max. Disk	3.33	2.28	4.8	10.42	6.46×10^7	2.08×10^8	5.82×10^6
			Receding Side				
Best Fit	149.6	1.0	0	7.73	9.91×10^7	0	2.23×10^9
Max. Halo	165.4	1.0	$\cdots$	8.55	0	0	2.50×10^9
Max. Disk	87.3	1.0	3.6	63.94	9.91×10^7	1.56×10^8	1.26×10^9

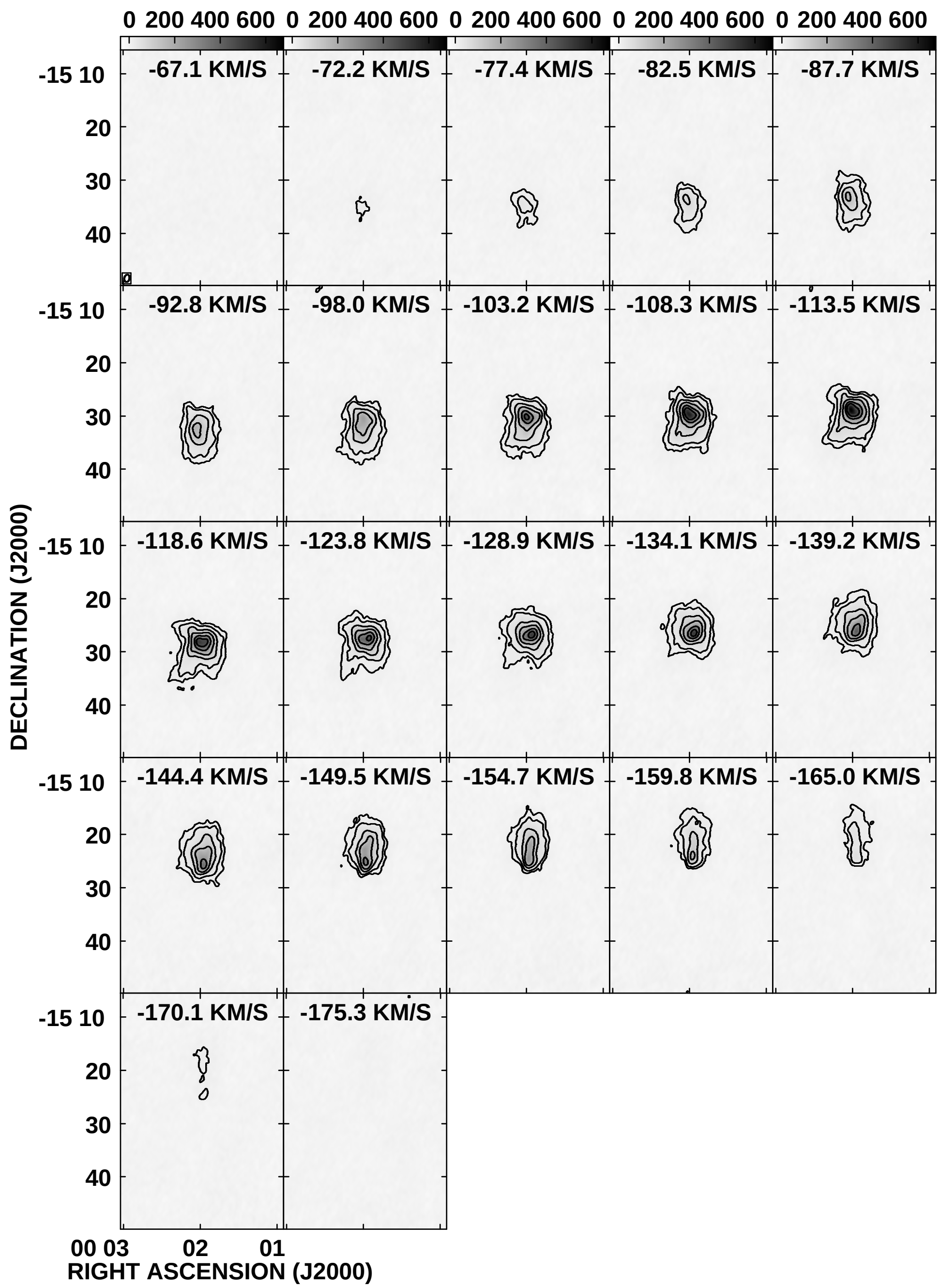

Fig. 1.— Emission in each channel for the naturally weighted D array mosaic of WLM. Every other channel is shown. The contours are 1, 2, 5, 10, 20, and 30 times the 3σ noise level (14.1 mJy beam^{-1}; 0.56K). The beam is given in the lower left hand corner of the first panel. The channel maps for the uniformly weighted D array mosaic of WLM are very similar.

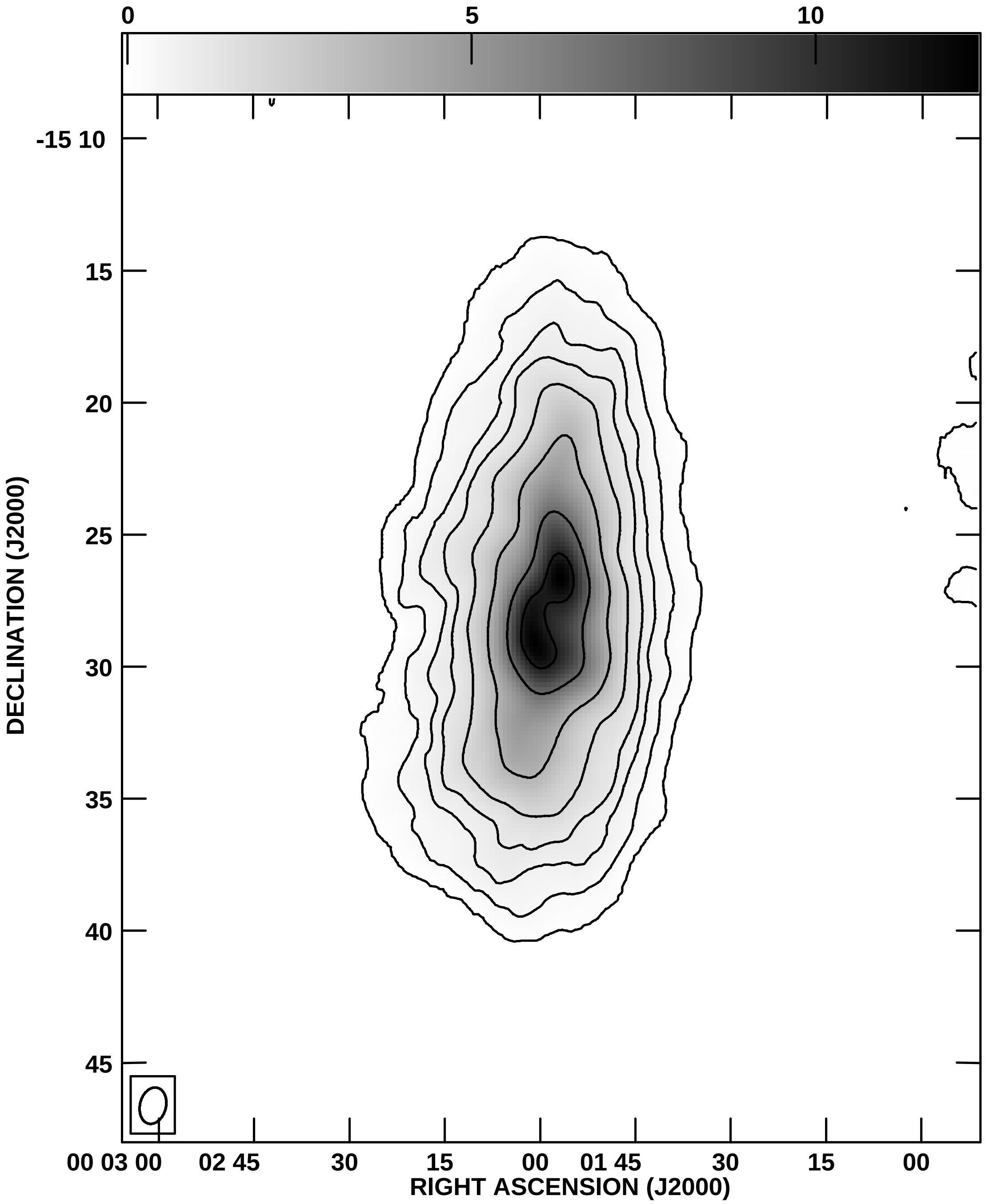

Fig. 2.— Integrated intensity map of WLM from the naturally weighted D array mosaic. The contour levels are 1, 10, 20, 30, 50, 100, 200, and 300 times the 3σ noise level (8.1×10^{18} cm^{-2}). The greyscale image is provided to help distinguish the contours. The emission at the edge of the plot is result of the mosaicking process (we have better sensitivity at the center of the image due to the overlap of pointings than at the edges) and is not real emission. Barnes & de Blok (2004) find no companion HI clouds near WLM with a detection limit of $1.9 \times 10^5 M_\odot$ for a object with a velocity dispersion of 10 km s^{-1} . The beam is given in the lower left hand corner of the image.

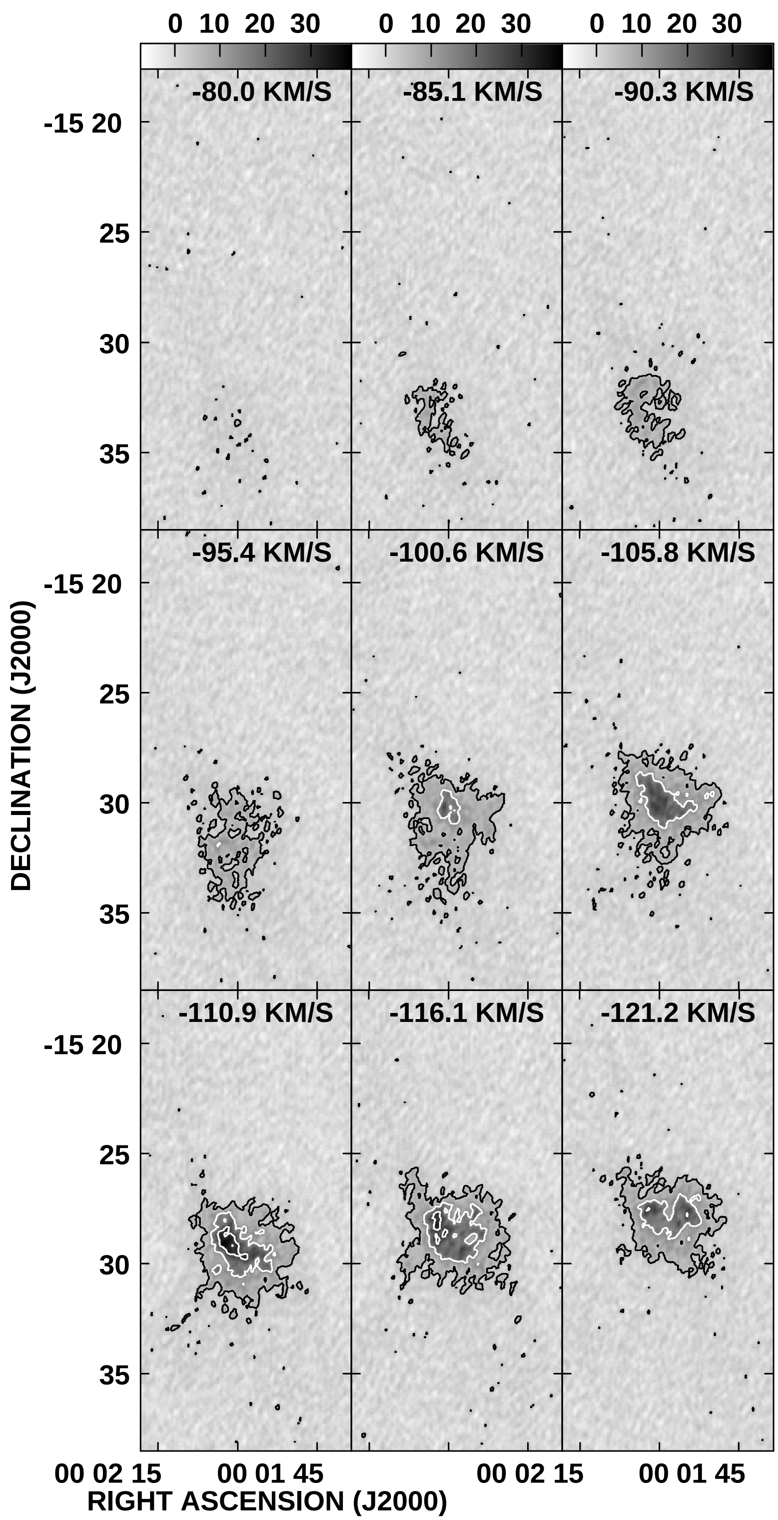

Fig. 3.— Emission in each channel for the B+C+D array cube. Every other channel is shown. The baryocentric velocity of the channel is in the upper right of each panel. The contours are for 3, 10, and 20σ emission. The 1σ noise is 1.4 mJy beam^{-1}, which is equal to 5.0K for our beam. The beam is shown in the last panel.

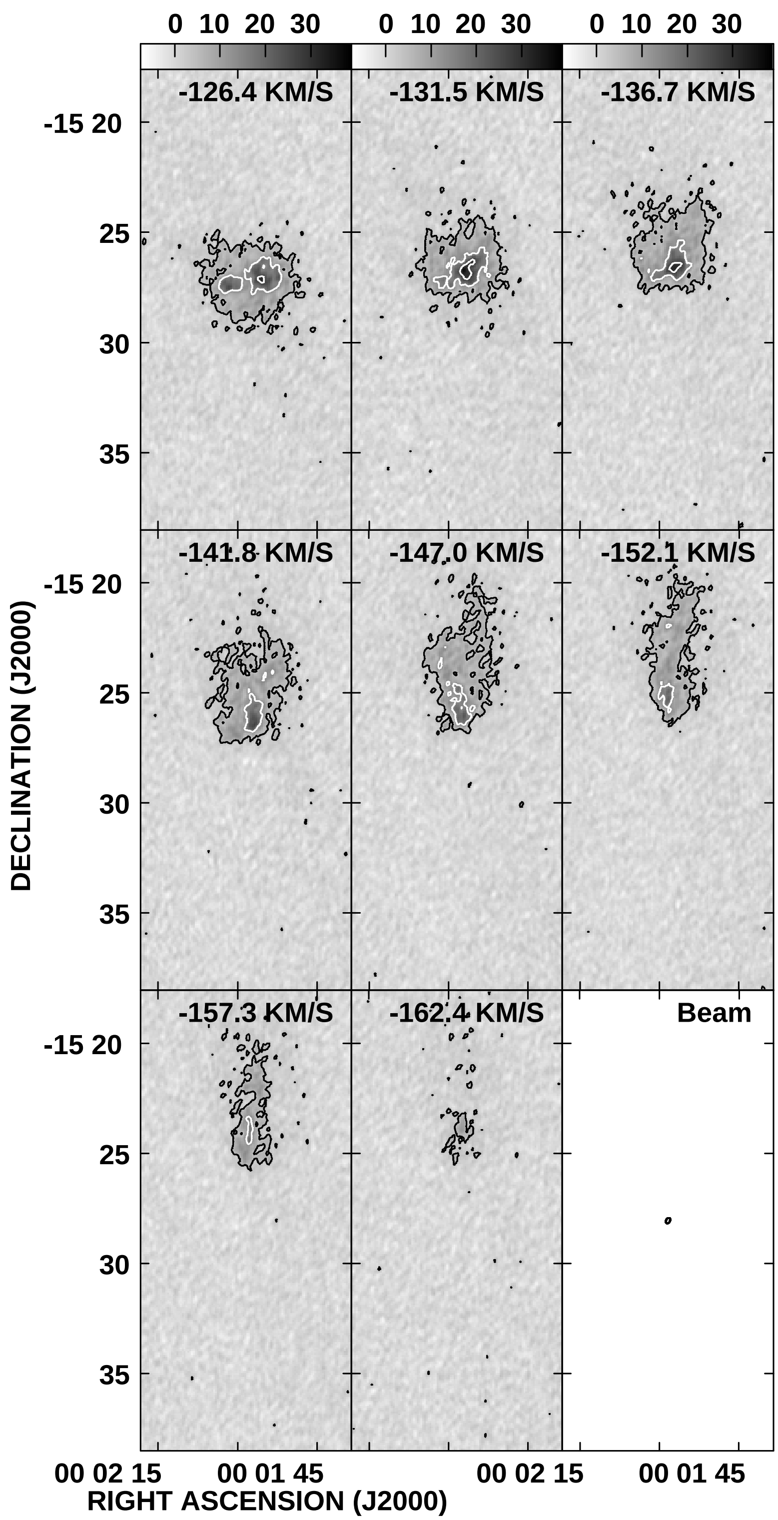

Fig. 3.— *Continued*

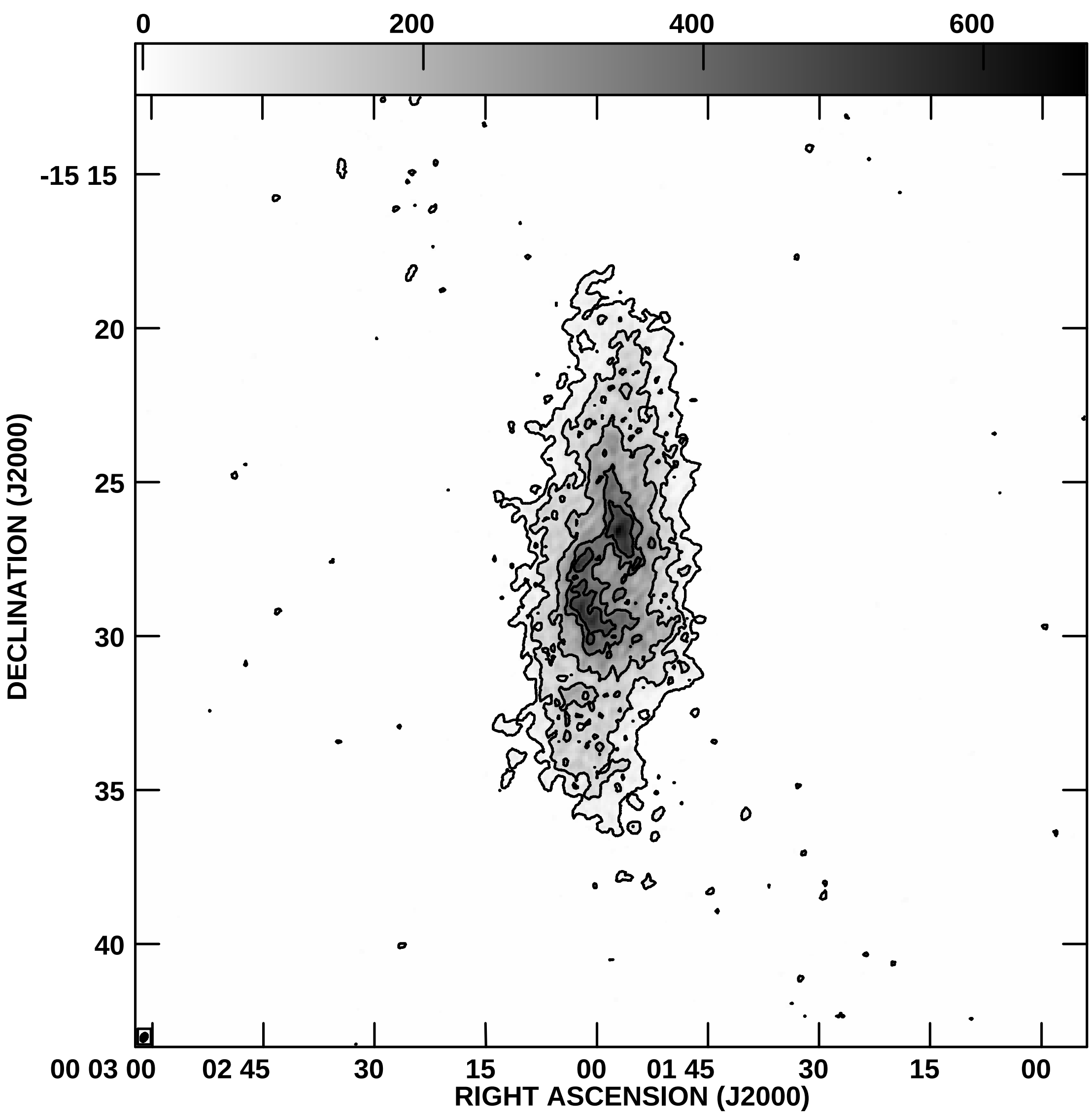

Fig. 4.— Integrated intensity (moment zero) map of WLM from the B+C+D array cube. The contour levels are 3, 20, 45, 90, and 120 times the 1σ noise level (2.9×10^{19} cm^{-2}). The greyscale image is provided to help distinguish the contours. The beam is shown in the lower left hand corner of the image.

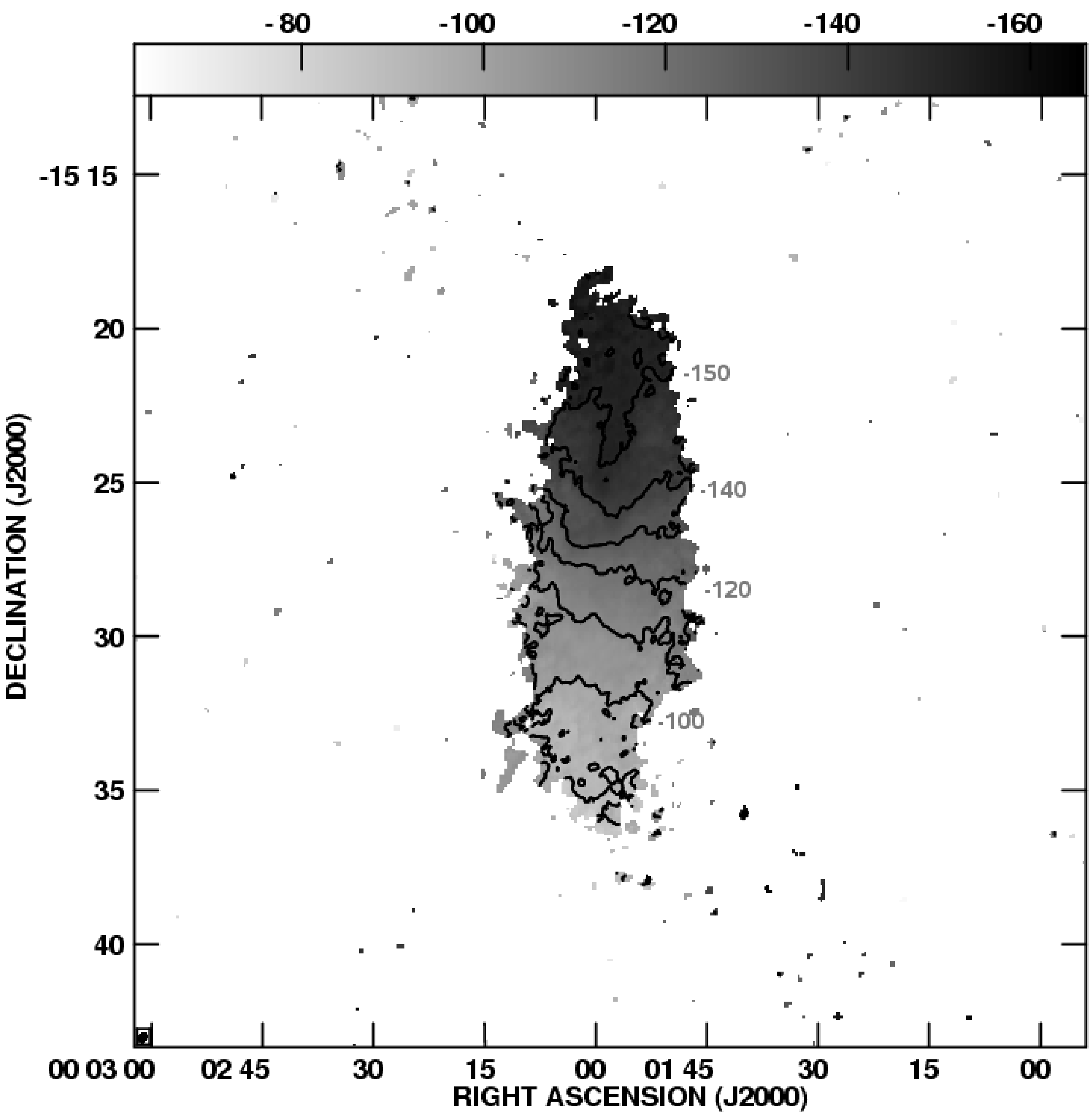

Fig. 5.— Mean velocity map (moment one) of WLM from the B+C+D array cube. The contour levels are -150, -140, -130, -120, -110, -100 and -90 km s^{-1} . The greyscale image is provided to help distinguish the contours. The beam is shown in the lower left hand corner of the image.

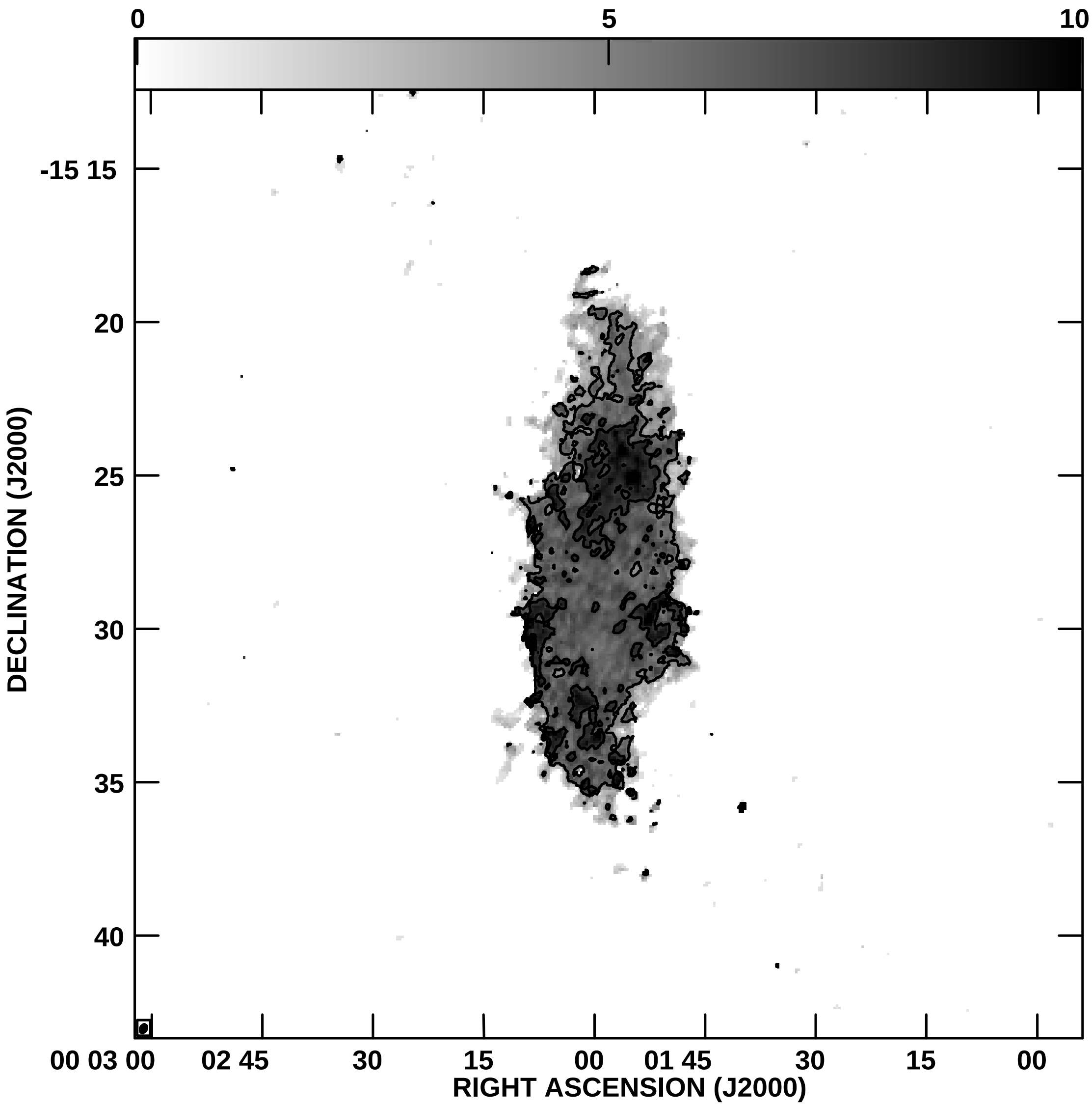

Fig. 6.— Velocity dispersion (moment 2) map of WLM from the B+C+D array cube. The contour levels are two and three times the width of one channel (2.57 km s^{-1}). The greyscale image is provided to help distinguish contours. The beam is shown in the lower left hand corner of the image.

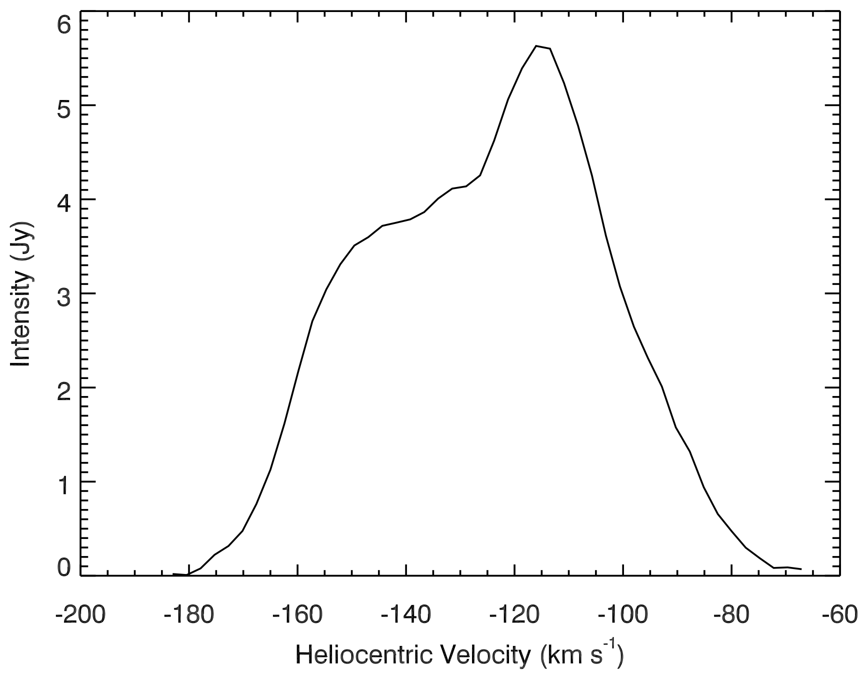

Fig. 7.— Integrated HI spectrum of WLM. The errors in this spectrum are on the order of the width of the plotted line.

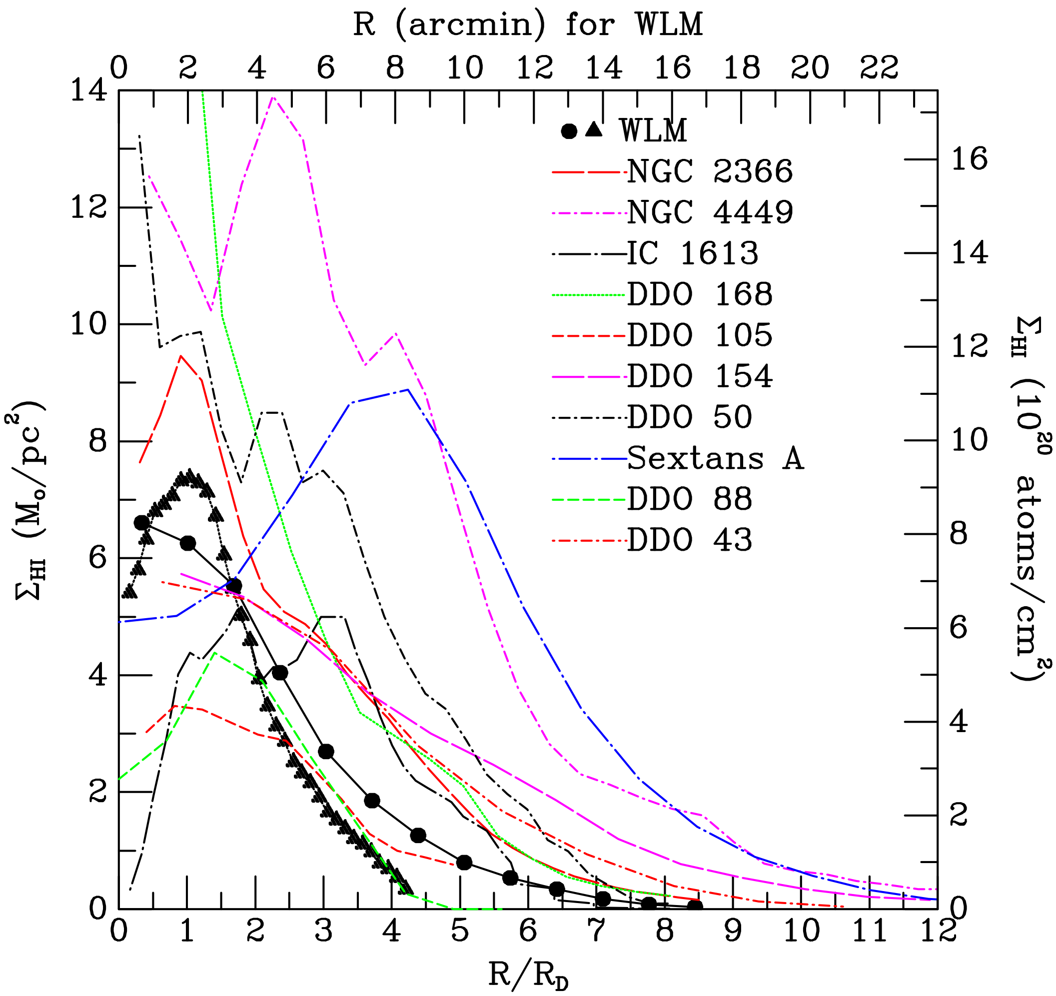

Fig. 8.— Surface density profile for WLM (black dots and black triangles connected with a solid black line) compared to the surface density profiles of other dwarf galaxies (colored lines). The black triangles show the surface density profile for the B+C+D array cube, while the black dots show the surface density profile for the naturally weighted D array mosaic cube. R_D is the V band disk scale length from Hunter & Elmegreen (2004). For WLM, $R_D = 2.0'$. The references for the surface density profiles of the other galaxies are: NGC 2366, Hunter et al. (2001); NGC 4449, Hunter et al. (1999); IC 1613, E.M. Wilcots (2001, private communication); DDO 105 and DDO 168, Broeils (1992); DDO 154, Carignan & Beaulieu (1989); DDO 50, Puche et al. (1992); DDO 88, Simpson et al. (2005a); and DDO 43, Simpson et al. (2005b).

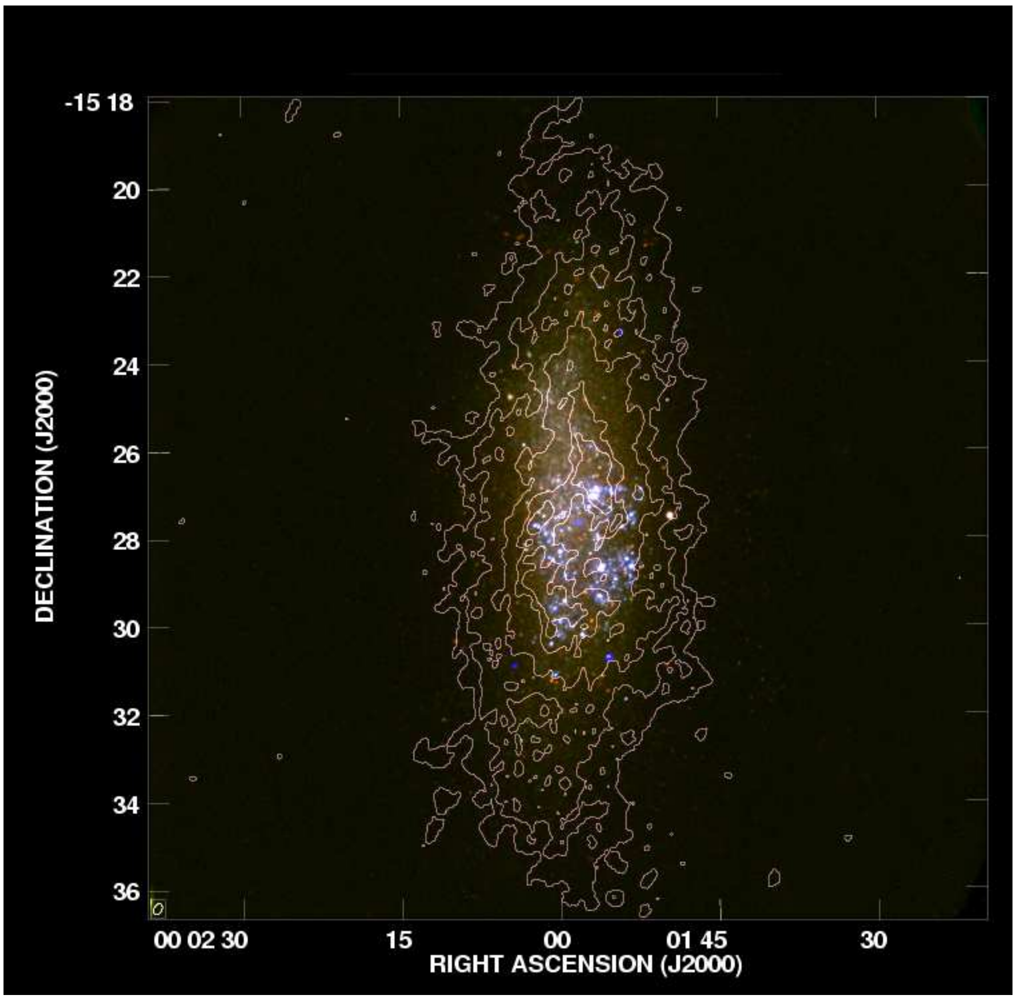

Fig. 9.— A combined color image of the UBV optical data with the HI contours from Figure 4 overlaid.

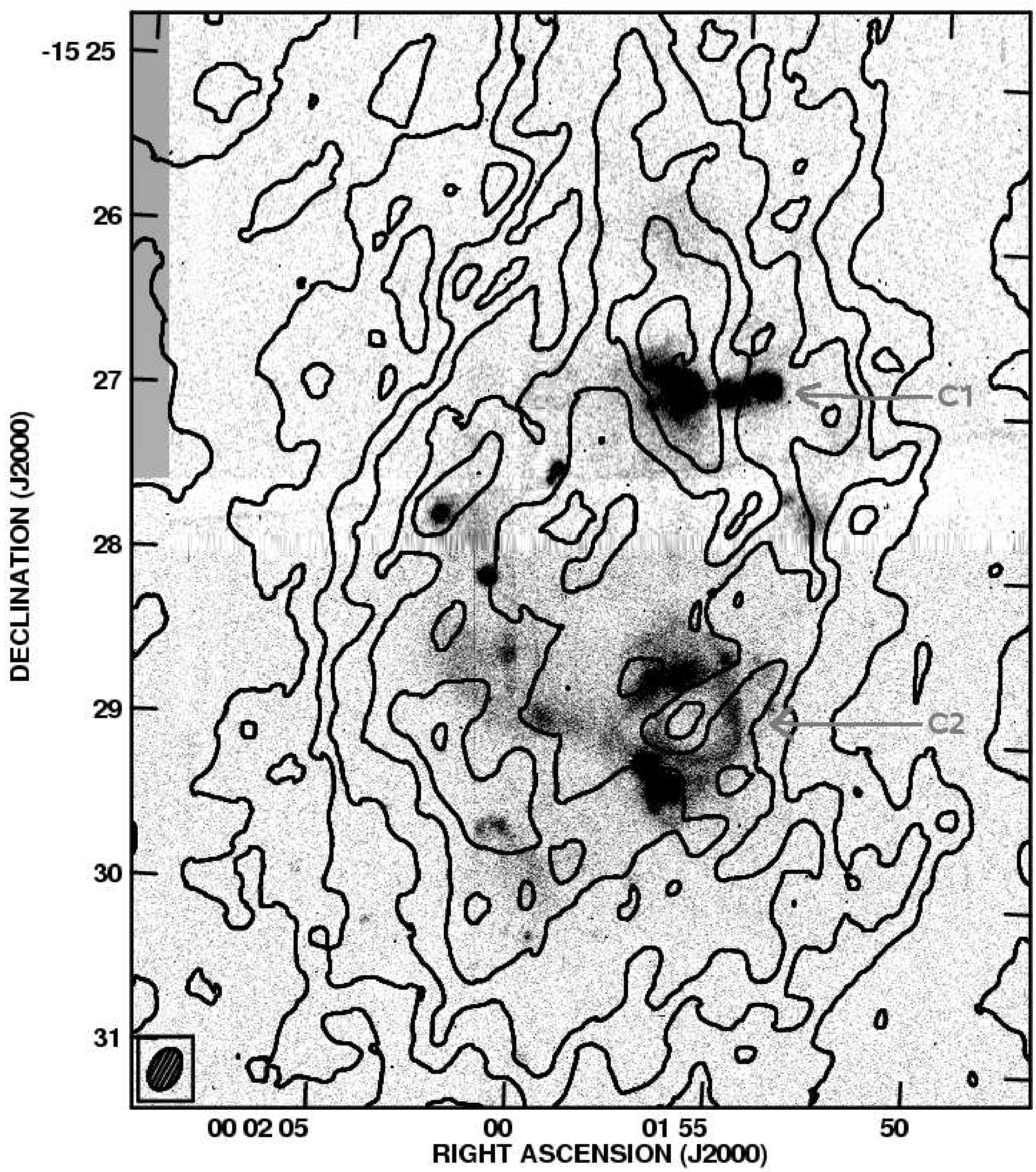

Fig. 10.— HI contours overlaid on the Hα image of WLM. The contour levels are 1, 30, 50, 70, 100, 130, 160 times the 1σ noise level ($2.9 \times 10^{19} \mathrm{cm}^{-2}$). The C1 and C2 H$\alpha$ complexes from Hodge & Miller (1995) are indicated by arrows.

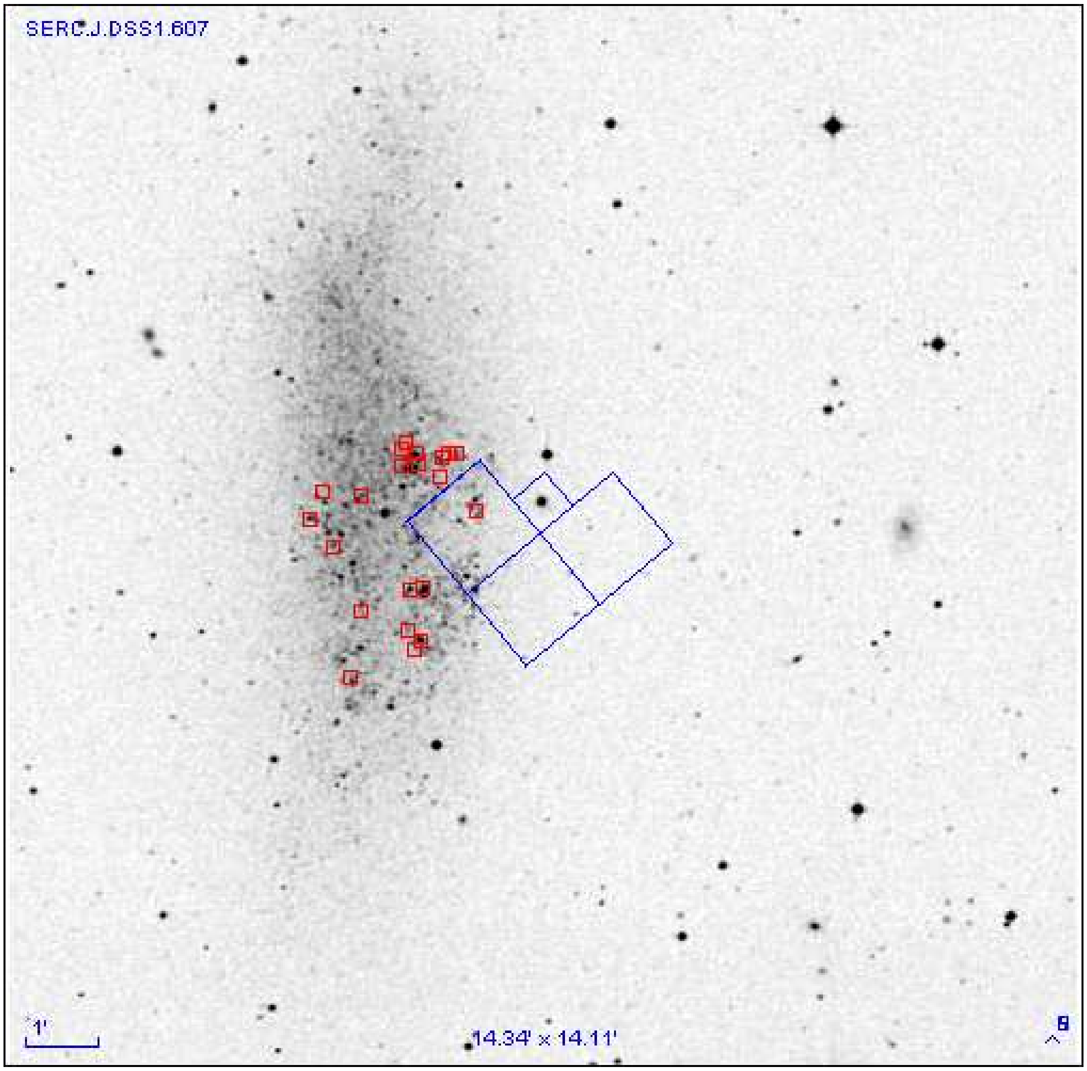

Fig. 11.— The location of the Dolphin (2000) HST WFPC2 fields overlaid on a DSS image of WLM. The red squares indicate the position of the Hα regions identified by Hodge & Miller (1995). The C1 and C2 complexes are directly north and south of the easternmost WFPC2 field. This image was created using Aladin (Bonnarel et al. 2000).

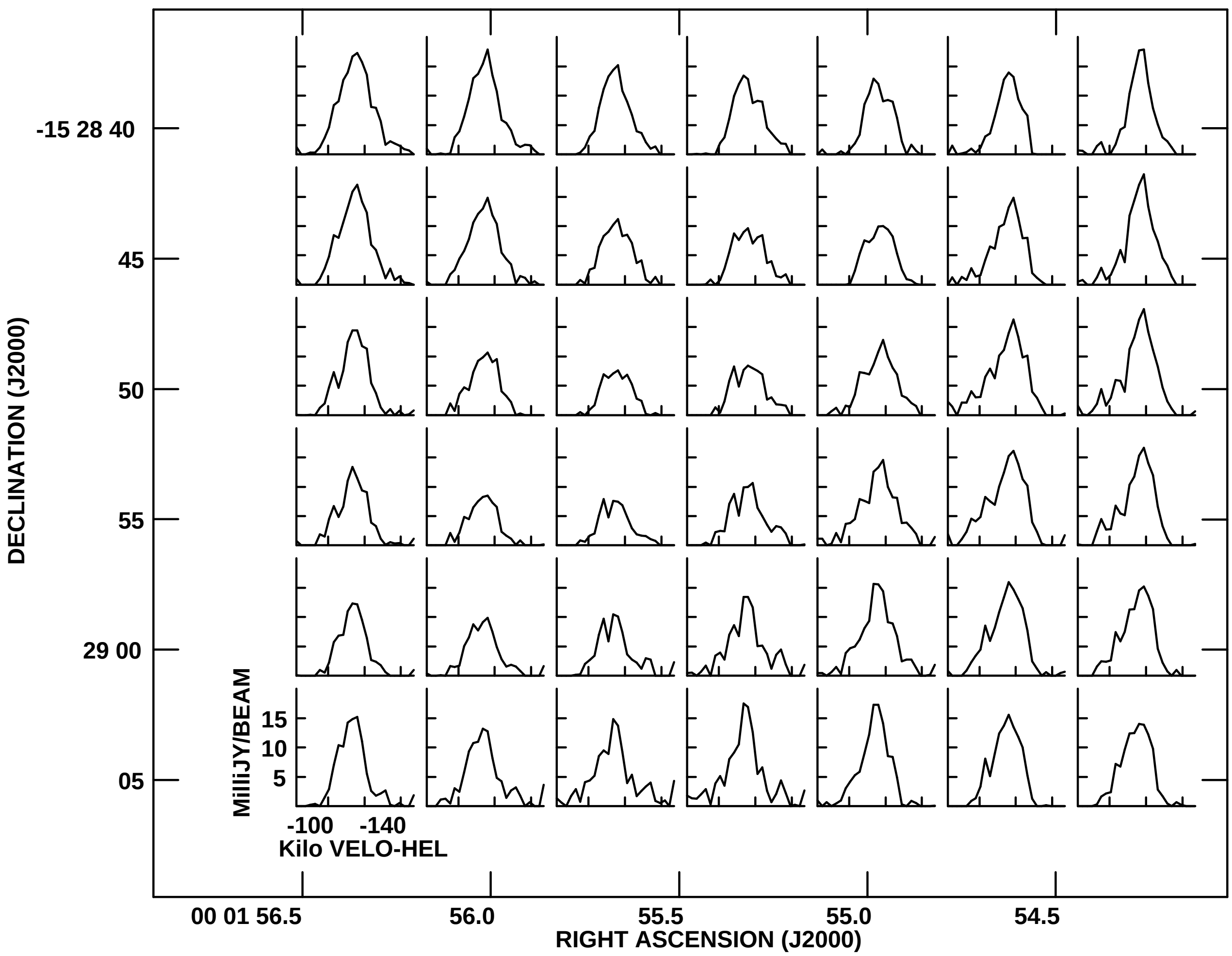

Fig. 12.— HI spectra for each pixel in the C2 Hα complex. Note the double peaked profiles near the center of the region. The separation between the two peaks is approximately 9 km s^{-1} , which gives an expansion velocity for the bubble of 4.5 km s^{-1} .

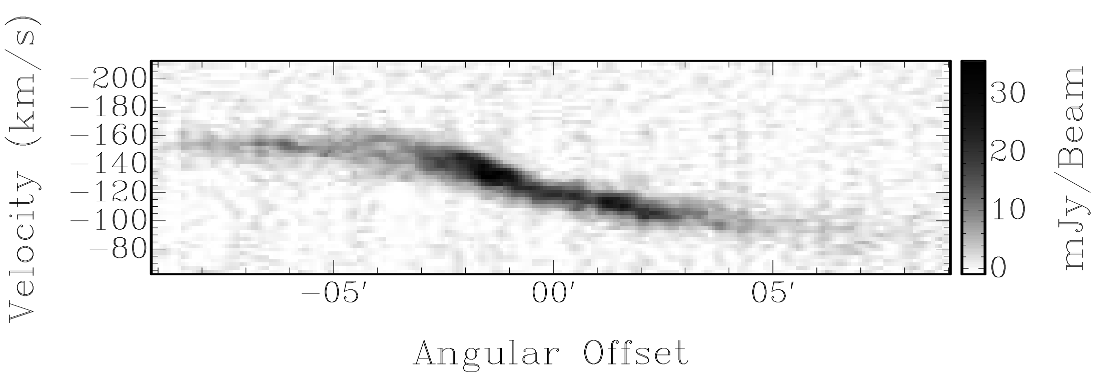

Fig. 13.— Position velocity diagram for a cut along the major axis of the neutral hydrogen distribution of WLM (PA = 179.6°, which is the position angle derived for the D array mosaic in Section 5). Positive offsets are along the receding axis and negative offsets are along the approaching axis.

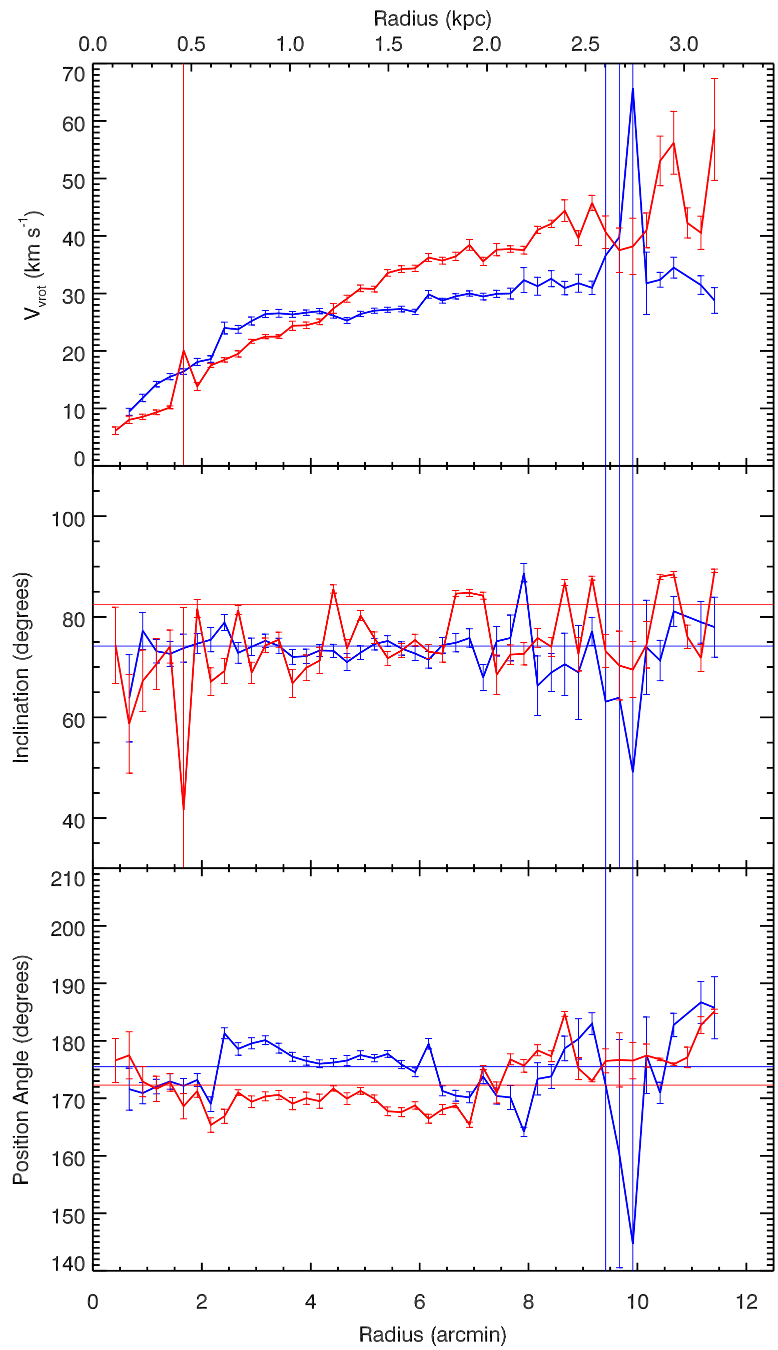

Fig. 14.— Summary of tilted ring model rotation curve fits. The top panel shows the rotation velocity as a function of radius, the middle panel shows the inclination as a function of radius, and the bottom panel shows the position angle as a function of radius. The two fits are shown in different colors: blue lines are for the fit to the approaching side of WLM using the B+C+D array cube and red lines are for the fit to the receding side of WLM using the B+C+D array cube. Error bars for each curve are shown in the corresponding color. The error bars for some points are quite large and extend vertically all the way across the graph. The thin solid lines running across the inclination and position angle plots are the weighted average of the inclinations and position angles for each fit.

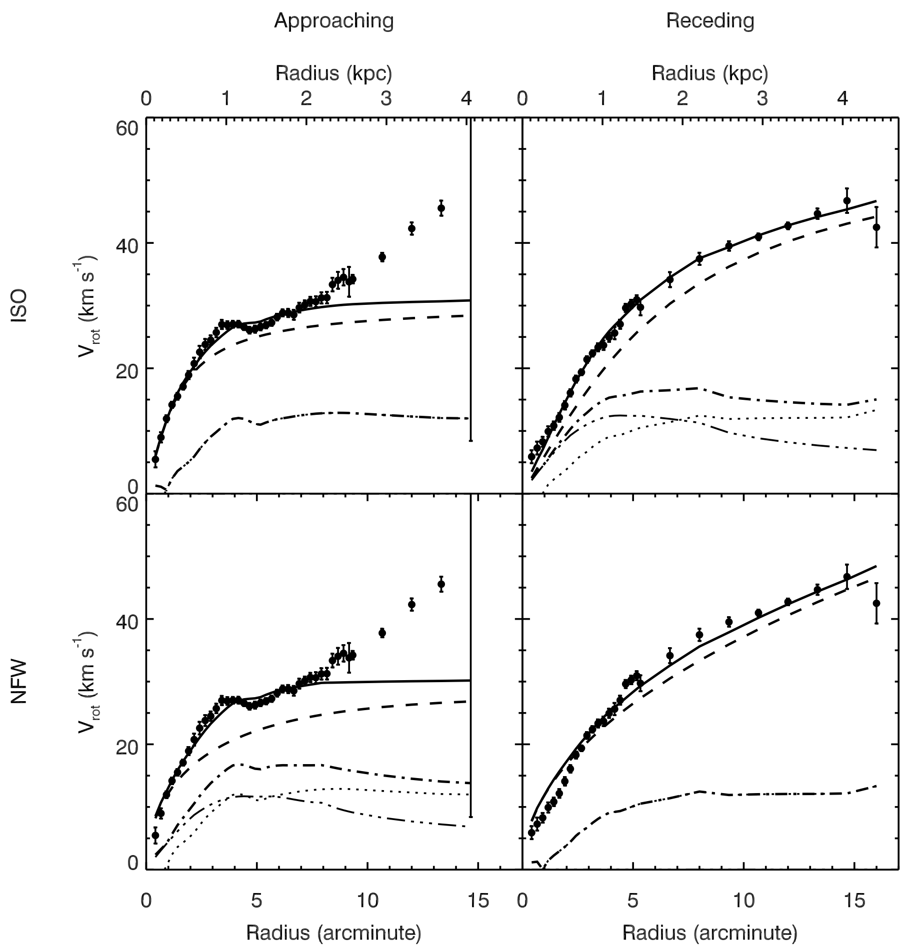

Fig. 15.— Best fit mass models for WLM. The left hand plots are for the approaching side of the galaxy and the right hand plots are for the receding side of the galaxy. The top row shows the fit for an isothermal sphere halo and the bottom row shows the fit for an NFW halo. The rotation curve is a combination of the B+C+D array and the D array mosaic rotation curves. The first two points were excluded from the fits to either side because they are the points most affected by inclination and beam smearing effects. Points at radii greater than $8'$ were excluded from the fit to the approaching side because beyond this radius the galaxy is warped and we are unable to constrain its inclination. The dashed line is the contribution to rotation curve from the best fit halo, the dotted line is the HI contribution, the dash-dot curve is the total disk contribution, and the solid line is the total rotation curve (disk plus halo). Note that because the derived M/L ratio of the disk is zero for some fits, the HI contribution and the total disk contribution lines overlap and there is no plotted contribution from the stellar distribution.